



The retrieval of aerosol optical properties based on a random forest machine learning approach: Exploration of geostationary satellite images



Fangwen Bao^{a,*}, Kai Huang^{b,*}, Shengbiao Wu^c

^a Department of Ocean Sciences and Engineering, Southern University of Science and Technology, Shenzhen, China

^b Honor Device Co., Ltd, Shenzhen, China

^c Division of Landscape Architecture, Department of Architecture, Faculty of Architecture, The University of Hong Kong, Hong Kong Special Administrative Region

ARTICLE INFO

Edited by Menghua Wang

Keywords:

Aerosol optical depth
Angstrom exponent
Random Forest
Himawari AHI

ABSTRACT

Aerosol optical properties are among the most fundamental parameters in atmospheric environmental studies. Satellite aerosols retrievals that are based on deep learning or machine learning approach have been widely discussed in remote sensing studies, but the flexible random forest (RF) model has not received much attention in the retrieval of geostationary satellite, like Himawari-8. Thus, the Himawari-8 aerosol retrieval achieved by RF model requires further investigation and optimization. Based on the radiative transfer equation, this study proposed a RF model driven by a differential operator, which quantifies a simple linear relationship between aerosol optical depth (AOD) and top-of-atmosphere (TOA) reflectance enhancement. The spectral information of aerosols is achieved by independent TOA reflectance comparison between images rather than one result from multiple band synthesis. The method allows simple feature inputs and shows weak dependence on auxiliary data. It also achieves simultaneous retrievals over different surfaces and maintains mathematical correlation between spectral AODs and Angstrom Exponents (AE). The model performance was evaluated using a series of comprehensive temporal and spatial validation analyses. A sample-based tenfold cross-validation (10-CV) shows that the new method can simultaneously improve the estimation of aerosol properties, with considerably high correlation coefficients (R^2) of 0.85 for AODs at the 0.50 μm wavelengths, a mean absolute error (MAE) of 0.08, a root mean square error (RMSE) of 0.13 and >70% of the samples fell within the AOD expected error (EE). The high accuracy of the spectral AOD retrievals also exhibits good performance on AE calculations, with at least 2/3 of the samples falling within the EE. The site based 10-CV also evaluates the spatial predictions on AODs at the 0.50 μm wavelength, with R^2 of 0.67, MAE of 0.12 and RMSE of 0.18. It also has outperformed the Himawari operational aerosol products and appeared to be comparable to other popular machine learning models with better AE retrievals in some typical regions. Two typical regional pollution cases also highlight the advantages of the new aerosol monitoring approach. The 5 km resolution aerosol retrievals exhibit good spatial coverage and performance when describing the regional pollution levels and types. The proposed method improves the performance of RF in retrieving aerosol properties from geostationary satellites and also offers a new prospective for aerosol remote sensing using machine learning approaches.

1. Introduction

Aerosol particles in the atmosphere significantly affect the Earth-atmosphere radiation balance by absorbing or scattering solar radiation (Charlson et al., 1992; Hansen et al., 1997; Ramanathan et al., 2001). Therefore, an accurate understanding of the spatial and temporal scales of aerosol concentrations and their properties has been an important focus in studies of the environmental and climate effects related to aerosols over the last 20 years. Aerosol optical depth (AOD) is

a parameter describing the total amount of solar extinction for the whole atmospheric layer and is the most basic and important optical parameter for aerosol remote sensing. It can be used not only to assess the impact aerosols have on radiative forcing (Myhre et al., 2013; Shindell et al., 2013; Yu et al., 2006) but also to obtain further estimations of the concentration of atmospheric particulate matter (Lee et al., 2011; Lin et al., 2015; Ma et al., 2016; van Donkelaar et al., 2010).

Satellite remote sensing measurements of the entering and leaving radiative flux at the top of the atmosphere are some of the most valuable

* Corresponding authors.

E-mail addresses: baofw@sustech.edu.cn (F. Bao), huangkai3@honor.com (K. Huang).

data available for climate change studies. In particular, geostationary orbiting satellites are sufficiently capable of acquiring aerosol changes at higher temporal resolution. It allowed to study large scale areas and make findings that cannot be done by in situ observations. The rapid development of satellite missions and sensors have led to continuous improvement and development in aerosol retrieval algorithms, among which algorithms based on physical models are particularly prevalent (Dubovik et al., 2011; Hsu et al., 2004; Jackson et al., 2013; Lee et al., 2010; Levy et al., 2013; Martonchik et al., 1998; Yumimoto et al., 2016). These algorithms use forward models predicated on radiative transfer theory and describe the entire process in which electromagnetic waves emitted from the sun are observed by remote satellite sensors (Vermote et al., 1997).

However, some issues have posed greater challenges to the mature satellite aerosol retrieval algorithms. The retrieval process operation is typically quite complicated since the radiative transfer monitoring process of satellite sensors is highly related to numerous parameters, such as atmospheric parameters (e.g., complex refraction index, spectral size distribution, AOD), surface parameters (e.g., reflectance, or the more complex bidirectional reflectance distribution function, BRDF), and observational geometry (e.g., solar and viewing angles). Usually, we should consider all possible scenarios in advance and construct lookup tables (LUTs) for these scenarios using the forward model to increase the efficiency of the inversion. However, establishing LUTs is also very time-consuming, and the inability of most satellites to provide multi-angle synoptic observations also limits us from constructing sufficiently refined LUTs for all undefined parameters. As a result, most studies based on non-AOD-dependent parameters in radiative transfer applied empirically derived aerosol physics and surface models to treat these parameters as known, which undoubtedly introduces another problem, reduced accuracy (Chu et al., 2002; Qin et al., 2021; Sayer et al., 2014). This is particularly evident in geostationary satellite algorithms, where studies have shown that geostationary satellite aerosol retrievals have large errors related to solar angles, especially during spring and winter afternoons (Zhang et al., 2019). Multi-angle satellite observations are an effective method to address the limitations imposed by traditional empirical models (Dubovik et al., 2011). These observations can retrieve multiple aerosol and surface parameters using statistically optimized solutions. However, this algorithm is less generalizable on single angle sensors and has a low computational efficiency. Therefore, improving the accuracy and efficiency of satellite aerosol retrievals is the most important issue to be addressed in current aerosol remote sensing research.

Due to the excellent ability of machine learning to predict variables using nonlinear fitting algorithms, these techniques have become popular for dealing with quantitative retrieval issues where the remote sensing mechanism is difficult to describe precisely (Hu et al., 2017; Stafoggia et al., 2019; Wei et al., 2019). For AOD, there are three main aspects of research related to improving the accuracy and efficiency of the inversion. One of these aspects is to train the neural network (NN) model using the ground-based Aerosol Robotic Network (AERONET) AOD and the radiation measurements from satellite images (Chen et al., 2020; Di Noia et al., 2017; Niang et al., 2006; She et al., 2020; Taylor et al., 2014). Another approach is to train the forward radiative transfer model directly using NN instead of the traditional LUT building process, which helps to improve the computational speed and accuracy of aerosol retrieval, especially for hyperspectral remote sensing data with large computational volumes (Fan et al., 2019; Nanda et al., 2019). In addition, some studies used NN to correct the current satellite AOD dataset to reduce the error by analyzing the possible influencing factors in the traditional method (Lanzaco et al., 2017; Lary et al., 2009; Vucetic et al., 2008).

Himawari-8 is next-generation geostationary satellite that provides high resolution images, which has great potential in monitoring spatial and temporal patterns of aerosols. Several studies have devoted to Himawari-8 aerosol products improvements using deep learning

approach. Refining AOD retrievals by constructing spectral surface reflectance relationship through NN in mature physical models have been demonstrated significant contributions (Su et al., 2020). But the accuracy is still constrained by geometries and surface assumptions. Developing an ensemble machine learning method for operational AOD improvements also worked well (Chen et al., 2022a; Jiang et al., 2019), but the model shows poor portability due to the strong dependence on initial AOD products. Retrieving aerosol directly from spectral measurements is free from these limitations. Chen et al. (2022b) proposed aerosol retrieval strategies using multi-band measurements of Himawari via independent NN approach, providing reasonable results of AOD (0.500 μm) and Angstrom exponent (AE) in China. Similar studies aimed at AOD retrievals (0.500 μm) were also tested by Chen et al. (2022c) and She et al. (2020) according to different input features of NN. Nevertheless, NN is widely used rather than Random Forest (RF) model because feature inputs suitable for RF has not been explored yet. RF models are more flexible and portable than NN, but the accuracy is much lower when using same inputs (She et al., 2020) and has not received much attention. Additionally, retrieving aerosol properties from Himawari-8 using RF approach still needs further optimization because a) consensus on RF feature selection for accuracy improvement remains difficult due to the lack of detailed interpretation; b) only one parameter can be obtained from multi-band observation or their combination, which is inconsistent with the inputs of mature physical models; c) spectral AODs retrievals is missing, and mathematical correlation is not considered between spectral AOD and AE retrievals; d) dependence on coarse auxiliary data prevent the model achieving finer retrievals.

In this study, we focus on investigating and optimizing a simple RF method to directly estimate spectral AOD and AE from Himawari-8 TOA measurements. The retrieval benefits from RF model driven by new input features to overcome issues of existing Himawari-8 machine learning methods, which has not been tested in the previous studies. We tried to find predictors from clear physical mechanism interpretations and formula derivations in an attempt to minimize the influence of temporal variability of surface, aerosol types, and meteorological variables during retrieval. It is expected that the model obtains spectral information of aerosols by independent TOA reflectance comparisons between images, rather than one result from multi-band synthesis. The method allows rapid acquisition of hourly continental and oceanic aerosol properties (spectral AOD and corresponding AE) without auxiliary products with coarse resolutions, which provides a new prospective for higher resolution aerosol remote sensing.

2. Datasets and preprocessing

2.1. Himawari AHI

Himawari-8, the next-generation geostationary satellite from the Japan Meteorological Agency (JMA), carries the Advanced Himawari Imager (AHI). This instrument provides measurements in 16 independent bands with central wavelengths from 0.46 to 13.3 μm. The visible-infrared bands (bands 1–6) commonly used for aerosol retrieval can be converted to albedo or reflectance data (Yumimoto et al., 2016). AHI Images are available at spatial resolutions from 0.5 to 2 km and provide complete coverage within its survey domain (60° N–60° S, 80° E–160° W) at short time intervals (10 min). The latest standard L1B data are available via www.eorc.jaxa.jp/ptree/index.html

Several spectral measurements and their combinations, as well as other auxiliary products, are required as main features in current aerosol machine learning studies (Kang et al., 2022; She et al., 2020). In this study, more emphasis is given to investigating a simple set of input features, with only spectral L1B images (at 0.46, 0.64 and 2.30 μm) and geometric information (solar zenith/azimuth and AHI zenith/azimuth) involved. The AOD values at red and blue wavelengths are retrieved by their independent corresponding observations of AHI, which is consistent with the physical retrieval algorithm and free from additional

auxiliary data and redundant empirical models.

2.2. AERONET AOD

AERONET is a globally distributed network widely used to characterize local aerosol optical properties (Holben et al., 1998). The network maintains historical records of >800 automated Cimel Electronique Sun-sky radiometers. Direct (collimated) solar radiation measurements are obtained every 15 min in seven spectral channels, providing information on columnar AOD. The latest version 3 algorithm processing includes three quality levels. The highest quality data can be found in version 3, level 2.0 AOD products, which require a final field calibration of the instruments, with an AOD uncertainty of 0.01–0.02 (Giles et al., 2019). In this study, AERONET AODs at 0.440 μm, 0.675 μm and corresponding AE (0.440 μm–0.675 μm) are used as true value for training and validating the machine learning model. AERONET AODs at 0.500 μm are also selected for comparing the overall accuracy against the Himawari-8 L2 aerosol properties products (L2ARP).

2.3. Data matching and processing

To illustrate the model validation and spatial prediction performance, Himawari AHI images of 2018 and relevant AERONET products within the AHI domain are selected. Here, we only select daytime records with a 1-h sampling interval from 22:00 UTC to 09:00 (day+1) according to the AHI imaging range. The AERONET AOD data were averaged over ±30 min window based on the AHI imaging time to reduce anomalous perturbations. The corresponding AHI spectral records used for model training were obtained from station coordinates. The pixels with cloud interference were removed by the Himawari L2 cloud product (Letu et al., 2020). Fig. A1 (Appendix) illustrates the amount of data available for machine learning from the AERONET sites within the AHI domain. It should be noted that the features from the satellite images of our model do not require a downsampling process that averages the n*n pixels over an AERONET site. The variations in AHI observation due to surface differences around the site are part of the model training that need to be considered.

3. Methodology

3.1. Start from forward radiative transfer equations

The main issue in current machine learning regarding aerosol remote sensing is that any variables can be added as input features during the training process. However, it is difficult to determine if duplicate physical mechanisms exist among the additional variables. Redundant features input can affect the physical interpretation of the training model, although the accuracy of the results may be high. Moreover, current machine learning AOD models are often trained independently over land and ocean due to the differences in surface inputs (or assumptions). Therefore, it is important to find a key input feature that can determine the final AOD without specific surface reflectance assumptions or products and ensuring consistency with the physical algorithm inputs.

TOA reflectance under polluted (ρ^p) and clear (ρ^c) conditions can be expressed as (Vermote et al., 1997):

$$\left\{ \begin{array}{l} \rho^p = \rho_0^p + F^p T^p \rho_{sur} / (1 - s^p \rho_{sur}) + \rho_r^p + \rho_g^p \\ \rho^c = \rho_0^c + F^c T^c \rho_{sur} / (1 - s^c \rho_{sur}) + \rho_r^c + \rho_g^c \end{array} \right. \quad (1)$$

where ρ_0 is the upward reflectance for surface reflectance $\rho_{sur} = 0$. F and T are the total downward and upward transmittance, respectively. s is the atmospheric backscattering ratio, which represents the fraction of the upward flux reflected back to the surface. Actually, $s\rho_{sur}$ is a smaller

value term and can therefore be ignored in the equations. ρ_r is the Rayleigh intrinsic reflectance (air molecules) and ρ_g is the gaseous contribution, such as H₂O, CO₂, O₂ and O₃.

Usually, the molecular and gaseous contributions change relatively slowly over time compared to the drastic changes in aerosols. Therefore, the difference between ρ^p and ρ^c is only affected by aerosol variations under the same geometries:

$$\Delta\rho = \rho^p - \rho^c = (\rho_0^p - \rho_0^c) + (F^p T^p - F^c T^c) \rho_{sur} \quad (2)$$

The aerosol radiance (ρ_0) and transmittance terms (FT) in Eq. (1) can be approximated by a linear relationship with AOD (τ_a). Thus,

$$\left\{ \begin{array}{l} \rho_0 = \delta \tau_a \\ \rho_s = \gamma \tau_a \rho_{sur} \end{array} \right. \quad (3)$$

here, δ and γ are linear coefficients, and they are both related to aerosol types, such as urban, biomass burning and dust aerosols, which have different scattering characteristics. When the aerosol types under different aerosol loadings are consistent, Eq. (2) is equivalent to

$$\Delta\rho = (\delta \tau_a^p - \delta \tau_a^c) + (\gamma \tau_a^p - \gamma \tau_a^c) \rho_{sur} = (\delta + \gamma \rho_{sur}) \Delta \tau_a \quad (4)$$

The AOD for polluted conditions (τ_a^p) is approximated by $\tau_a^c + \Delta \tau_a$.

Eq. (4) expresses a simple linearity between the TOA reflectance enhancement and AOD variations, which can be viewed as an aerosol retrieval feature (we call it Differential Operators) that offers both mathematical simplicity and physical completeness. Although many simplifications are used on the forward radiative transfer model, these simplifications actually have little effect on the difference operator calculation (Fig. A2 in Appendix). The differential operator has the following benefits in aerosol retrievals:

- This method ultimately resolves the AOD retrieval issues by addressing the impact of AOD on TOA reflectance enhancement. This can greatly simplify the problem of ground-aerosol coupling present in traditional physical algorithms and reduces the error introduced by empirical models.
- Since the differential operators require that the calculations occur within the same geometry, the operator is highly suited for geostationary satellites, which have a constant observation geometry for each pixel. However, it should be noted here that a small variation of solar geometry exists between hazy images and clear reference (maximum to 5° and 3° in solar zenith/azimuth variations), which can be essentially ignored in differential operator.
- The differential operators can also reduce the dependence on the meteorological and gaseous parameters and address the inconsistent data scales introduced by different products incorporated into machine learning models.
- The surface term weakly contributes to the difference operator, which is spatially heterogeneous but relatively stable at certain times. Since the spatial heterogeneity can also be expressed by the clear TOA reflectance, it is not necessary to accurately characterize the surface reflectance in the regression (e.g., by adding an empirical model). This allows the operator to facilitate the simultaneous retrieval of the AOD over land and ocean.

3.2. Considering the temporal and spatial differences in aerosol type

The temporal and spatial heterogeneity of the aerosol type-dependent coefficients (δ and γ in Eq. (4)) is very significant due to the large differences in pollution sources and geographical features. Geolocation of a pixel is usually adopted as a predictor that supports the aerosol type with spatial characteristics. However, it cannot define the seasonal variability. The seasonality may be represented by the temporal parameters, but the spatial pattern is missing. In this study, mature physical models were referenced, which use the clustered aerosol types as input features.

Clustering AERONET inversion products is a commonly used method to obtain microphysical parameters of aerosol types (Giles et al., 2012; Omar et al., 2005). In this study, k-means clustering is used to analyze the pollution types in different regions. Bao et al. (2016) pointed out that the radiation signal received by satellite sensors consists mainly of surface reflectance, while the signal of aerosols is extremely low during clear conditions, the types of which do not significantly affect TOA reflectance. As the level of pollution rises (AOD increases), the back-scattered signal of aerosols may gradually enhance or obscure the reflected radiation from the surfaces. Thus, the TOA reflectance differences among different aerosol types gradually become evident.

In this study, cluster analyses are proposed using AERONET inversion level 2.0 data due to their higher accuracy, although records are only accessed for larger AODs (https://aeronet.gsfc.nasa.gov/new_web/Documents/U27_summary_final.pdf). The optical-physical parameters selected for clustering are spectral single scattering albedo (SSA), refractive indexes (RI, including imaginary and real components) and multimodal log-normal distributions (including volume median radius and geometric standard deviations for fine and coarse models, respectively). The clustered aerosol models, categorized into Urban, Forest, Agriculture, Dust and Marine, are initially divided based on the seasons, potential pollutants, and locations. The models are combined into one category if the variations are not pronounced (such as dust in north-western China, sea salt over the ocean, and clear aerosols in Australia). A longer data range (2008–2018) is selected for clustering, ensuring that more pollution types can be considered. The spatial continuous properties of aerosol model will be obtained by kriging interpolation. The clustering sites as well as an example of kriging interpolated patterns is shown in Fig. 1. The optical-physical parameters of each cluster are shown in Appendix Tables A1-A4. Noted that since AE implies some information about the aerosol types and is known to have a strong relationship with the volumetric concentration fractions of fine particles (Schuster et al., 2006), the clustered volumetric concentration is not selected as the feature input. Additionally, since aerosol model is steadily influenced by aerosol of both natural and anthropogenic origins and presents persistently even in space, the spatial interpolation can be constrained by land use. For example, aerosol retrievals over deep ocean

will be forced to use the type ‘Marine’. A buffer of about 5° exists to ensure that plumes over ocean can receive the constraints of the continental aerosol models.

3.3. Clear reference from AHI images

AOD estimations using differential operators require a prior definition of clear images, which also contain key information on the spatial heterogeneity of the surface reflectance. Taking advantages of geostationary observation, clear reference images are obtained using the synthesis of TOA apparent reflectance from 30-day observations, which is also a common approach adopted in mature aerosol algorithms (Choi et al., 2016; Hsu et al., 2004; Lim et al., 2018; Lyapustin et al., 2018). The synthesis method determines the clear TOA reflectance values by finding the possible lowest AOD at a given pixels without clouds.

Appendix Fig. A3a-b shows simulations of the AHI TOA apparent reflectance under different AOD scenarios and aerosol models. It can be clearly seen that the backward scattering of aerosols can lead to an increase in the upward TOA reflectance on dark surfaces. In contrast, for bright surfaces, AOD shows a negative effect on TOA reflectance. The upward TOA reflectance decreases with increasing AOD. Thus, a critical value is easily found where the AOD contribution is approximately zero (which we usually refer to as the critical reflectance). However, the critical reflectance is not the same for different aerosol types. Appendix Fig. A3c-d shows the values of the critical reflectance that correspond to each of the above aerosol types at all geometries. Assuming at least one clear pixel without clouds and/or aerosols over a certain period (e.g., 30 days) when all (or most) of the AHI TOA observations during that period are lower than the critical reflectance, the second lowest value (to avoid cloud shadows) observed by the satellite can be considered a clear TOA reference. When all (or most) AHI TOA observations during that period are larger than the corresponding critical reflectance, we select the second largest one (to avoid cloud contamination) as the clear reference. It should be noted here that the clear reference image needs to be synthesized on an hourly scale. This draws on the advantage of the geometric stability of geostationary satellites, which can reduce biases due to the solar zenith as well as the directional reflectance of the surfaces

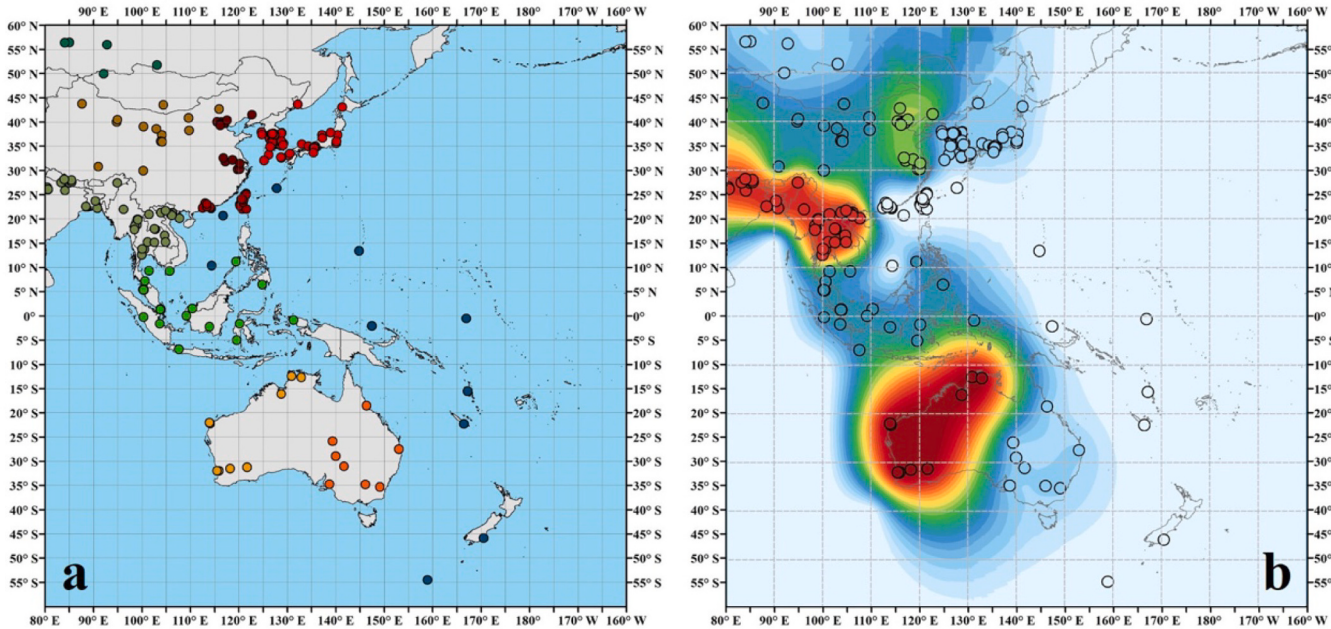


Fig. 1. (a) The clustered aerosol models in the AHI domain (80°E-160°W, 60°N-60°S). (b) Aerosol Model interpolated by Kriging (SSA at 0.675 μm is applied as an example). The circles represent the AERONET sites.

defined by BRDF.

Additionally, aerosol model is steadily influenced by the origins and low AOD presents persistently even on clear days. However, they still present spatial heterogeneity in the whole AHI domain. Apart from being used for clustering, the long-term AERONET measurements were also used to statistically determine the background aerosol values of each model, corresponding to the monthly minimum spectral AOD. Fig. 2 shows the clear reference AOD selected from the AERONET measurements of each clustered aerosol model. The value ranges from 0.02 and 0.22, which attribute to the local atmospheric conditions, metrological environment, and pollution levels.

3.4. Random forest model

The random forest (RF) model is a highly flexible machine learning approach that integrates multiple binary decision trees. Each of these decision trees is constructed using a randomized training scheme, which selects feature-generating nodes for sample division and makes independent training and judgments. The optimal split node in a binary tree can be selected by the minimum of the loss function (Hastie et al., 2009):

$$C = \sum_{x_i \in R_1} (y_i - \hat{c}_1)^2 + \sum_{x_i \in R_2} (y_i - \hat{c}_2)^2 \quad (5)$$

where:

$$\hat{c}_1 = \text{mean}(y_i | x_i \in R_1), \hat{c}_2 = \text{mean}(y_i | x_i \in R_2) \quad (6)$$

where (x_i, y_i) are the samples for training. R_1 and R_2 are the two subsets split by the current node.

The basis of the RF model is to select the results of several weak classifiers to form a strong classifier, which integrates the predictions of all decision trees into a single output (voting for classification issues and averaging for regression issues). RF provides multivariate, nonparametric, nonlinear regression and classification based on training datasets, with greater training efficiency that can be reliably tuned to the required accuracy and available computational resources. It can efficiently process multiple input variables without the necessity of downscaling and normalization (Breiman, 2001).

The RF model has been reported previously for applications in particulate matter estimation (Hu et al., 2017; Huang et al., 2018; Stafoggia et al., 2019; Wei et al., 2019). However, there are far fewer applications in AOD remote sensing since they are not as accurate as NN models with the same feature inputs. To further improve the interpretation of the RF model on AOD estimation, a random forest AOD prediction approach based on the differential operator described in section 3.1 is developed

(abbreviated as DORF). The model inherits from the mature physical inputs and benefits from the rich physics information in the differential operator and has the potential to retrieve the AOD values over land and ocean simultaneously.

To reduce the spatial bias introduced between AERONET sites and the AHI image, a window range of 5×5 AHI pixels around the AERONET location is selected, and the actual deformed differential operator ($\Delta\rho'$) used in the RF model is:

$$\Delta\rho' = \sqrt{\sum_{i=1}^n (\Delta\rho_i)^2} / n \quad (7)$$

where n is the number of valid pixels in a window. $\Delta\rho_i$ is the differential operator for each valid pixel. We applied sum of squares here rather than direct averaging to avoid counteracting differential factors with opposite signs before and after the critical reflectance.

The input features and outputs used in the DORF method are summarized in Table 1. Fig. 3 illustrates the structure and specific schematics of the DORF model. Independent prediction of multiple bands helps to further calculate the Angstrom exponent (AE) of the aerosol (α), which is a useful tool for extrapolating aerosol particle size (Ångström, 1929):

$$\tau(\lambda) = \beta\lambda^{-\alpha} \quad (8)$$

Table 1

The features and outputs used in the DORF model.

Input Features	Differential Operator	$\Delta\rho'(0.46)$	$\Delta\rho'(0.64)$
Clear AOD	$\tau_c(0.46)$	$\tau_c(0.46)$	$\tau_c(0.46)$
Solar Zenith	θ_0	θ_0	θ_0
AHI Zenith	θ_s	θ_s	θ_s
Relative Azimuth	φ	φ	φ
Refractive Index (Real Part)	$n(0.44)$	$n(0.64)$	$n(0.64)$
Refractive Index (Imaginary Part)	$k(0.44)$	$k(0.64)$	$k(0.64)$
Single Scattering Albedo	$\omega(0.44)$	$\omega(0.64)$	$\omega(0.64)$
Median Radius (Fine mode)	$r_{m, f}$	$r_{m, f}$	$r_{m, f}$
Geometric Standard Deviation (Fine mode)	σ_f	σ_f	σ_f
Median Radius (Coarse mode)	$r_{m, c}$	$r_{m, c}$	$r_{m, c}$
Geometric Standard Deviation (Coarse mode)	σ_c	σ_c	σ_c
Geolocation	Lat., Lon.	Lat., Lon.	Lat., Lon.
Date and Time (Month, Date & Hour)	mm, dd, hh	mm, dd, hh	mm, dd, hh
Output	AOD	$\tau(0.46)$	$\tau(0.64)$
	Angstrom Exponent	α	α

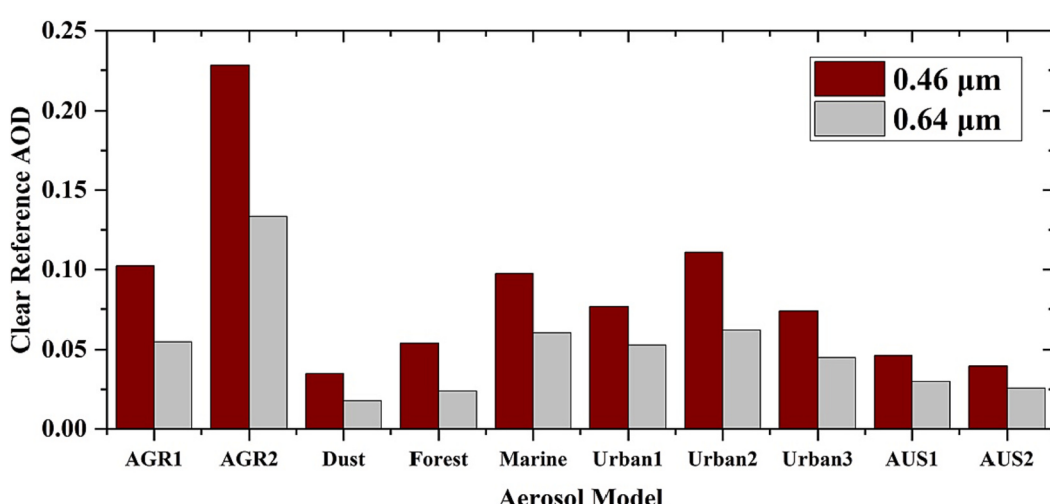


Fig. 2. Clear AOD of 2018 from the AERONET measurements of each clustered model.

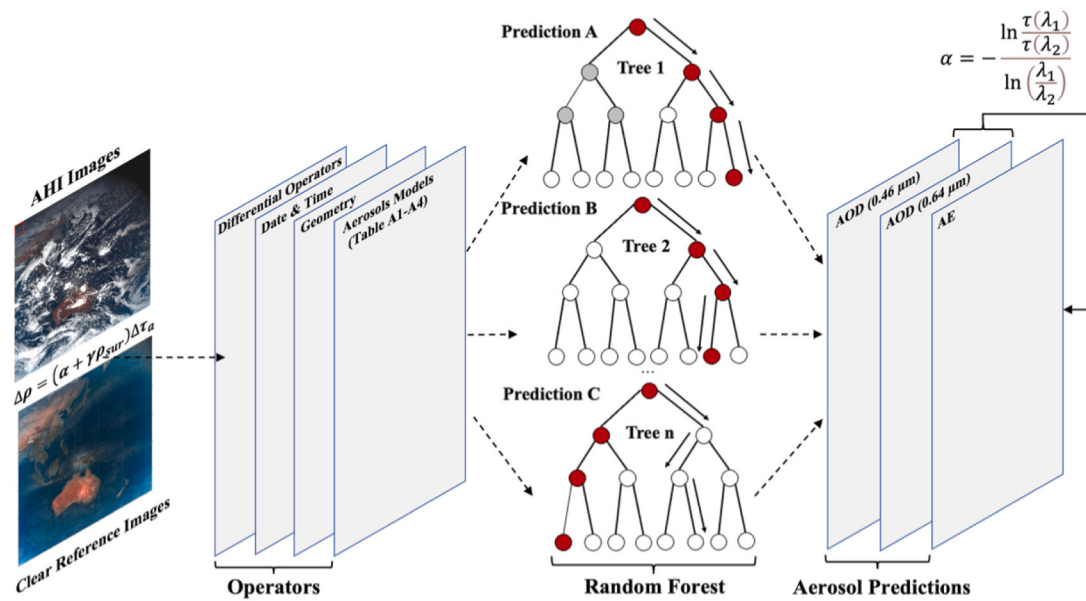


Fig. 3. The schematics of the multi-input DORF of AHI AOD and AE prediction.

where $\tau(\lambda)$ is the AOD at wavelength λ and β is the turbidity coefficient. AOD measurements at two different wavelengths allow the experimental determination of α according to:

$$\frac{\tau(\lambda_1)}{\tau(\lambda_2)} = \left(\frac{\lambda_1}{\lambda_2}\right)^{-\alpha} \text{ and further } \alpha = -\frac{\ln \frac{\tau(\lambda_1)}{\tau(\lambda_2)}}{\ln \left(\frac{\lambda_1}{\lambda_2}\right)} \quad (9)$$

4. Results and discussion

4.1. Importance measures of variables

A feature of the RF model is providing importance measures to gauge

the predictive strength of each variable, resulting in highly interpretive results compared with other machine learning models (Hu et al., 2017). The importance of each input features at 0.46 μm and 0.64 μm is depicted in Fig. 4. The contributions of the differential factors for the two wavelengths are 32% and 22%, respectively. This is followed by the clear AOD and AHI zenith, which totally accounts for 22% and 28%, respectively. This further confirms that the correction of clear AOD by difference factor under different angular observations is an important variable in prediction, which is consistent with the conclusion derived from the radiative transfer equation above. The variable importance is then followed by geolocation of pixels, date information (month and date) and solar zenith angle. The importance of these six parameters accounts for approximately 85% of all contributions and plays a decisive

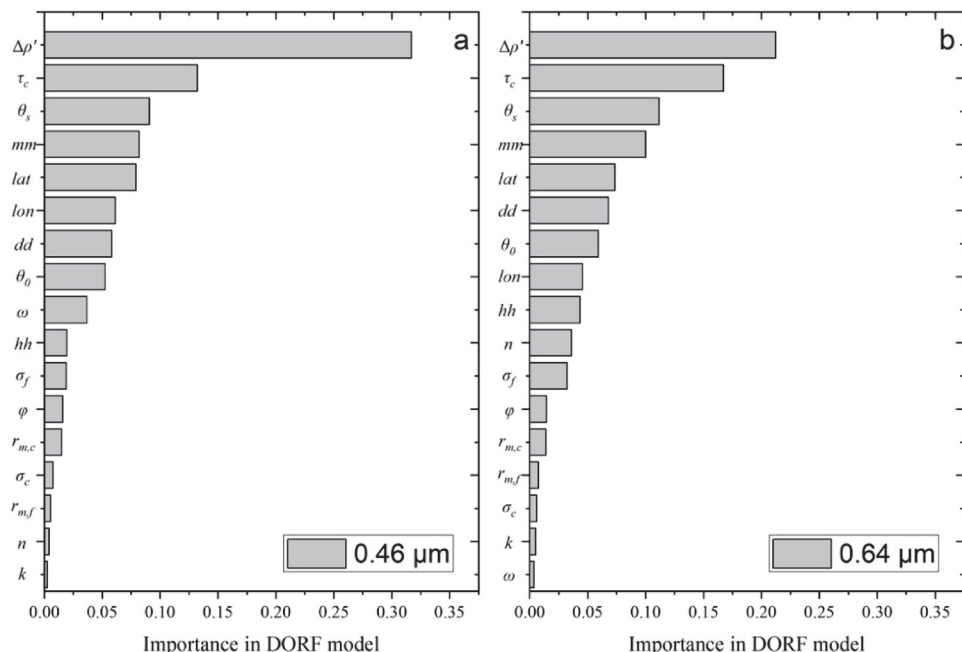


Fig. 4. The importance measures of each input in DORF. (a) at 0.46 μm and (b) at 0.64 μm .

role in determining the AOD value and its accuracy. Other parameters of aerosol models account for the remaining 15%. The low contribution also indicates a minimal role in AOD prediction.

4.2. General validation of DORF

4.2.1. Evaluation method and metrics

The robustness and generalization ability of the DORF model are tested by sample based tenfold cross-validation (10-CV), which randomly selects 90% of the samples for modeling and uses the remaining 10% for validation. This process is repeated 10 times to ensure that all samples are tested. The spatial predictive capability needs more independent validation to demonstrate the accuracy of the model over the areas without AERONET truth. Sited based 10-CV is applied, which performs the 10-CV process with 10% of AERONET sites randomly dropped from the training.

Some statistical parameters are used, such as the correlation coefficient (R^2), mean absolute error (MAE), and root mean square error (RMSE), to demonstrate the accuracy. Moreover, the standard expected error (EE) limits are also used to count the proportion of samples falling

within the EE. For AOD, we refer to the Moderate Resolution Imaging Spectroradiometer (MODIS) EE of $\pm 0.15\text{AOD} + 0.05$ and for AE, we use $\text{AE} \pm 0.4$. An all-around evaluation is proposed in the temporal (seasonal and hourly) and spatial (aerosol types and site scaled) phases.

4.2.2. Overall performance of the DORF model

Fig. 5 illustrates the overall performance of the DORF models. The modeling results (Fig. 5a-c) indicate that the DORF model is robust. For all 34,321 training samples matched with AERONET, both AODs at 0.46 μm and 0.64 μm have very high correlations, with an R^2 of 0.98, MAE of 0.03 and 0.02, RMSE of 0.05 and 0.04, and nearly 96% and 97% of the samples fall within the EE of the AOD, respectively. The wavelength indices AE calculated from the spectral AOD also showed good performance, with R^2 of 0.60, MAE of 0.17, RMSE of 0.27, and 87% of the samples falling within the EE. Since AE characterizes aerosol types to some extent, the results also show the potential of DORF-based AOD in identifying aerosol types.

Sample based 10-CV shows that the new method can improve the estimation of aerosol properties. With a large number of test samples, a fairly high and encouraging correlation coefficient can be found for

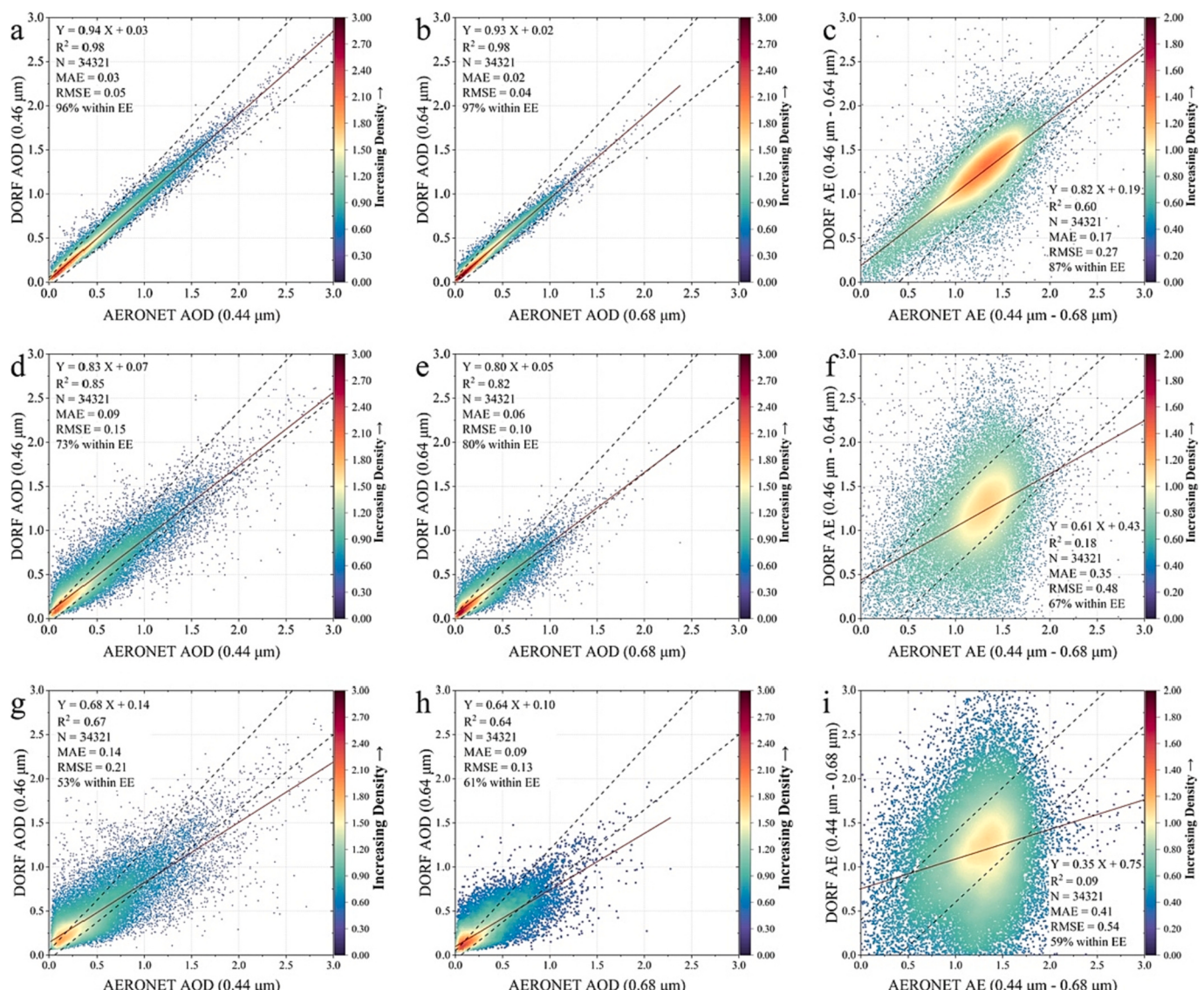


Fig. 5. Density scatterplots of modeling (a-c), sample-based 10-CV (d-f) and site-based 10-CV (g-i) of DORF aerosol properties. The red solid line and black dashed lines represent the linear regression and expected error, respectively. (For interpretation of the references to color in this figure legend, the reader is referred to the web version of this article.)

AODs at 0.46 μm ($R^2 = 0.85$) and 0.64 μm ($R^2 = 0.82$), with MAE ≤ 0.10 (0.09 and 0.06, respectively), RMSE ≤ 0.15 (0.15 and 0.10, respectively), and >70% (73% and 80%, respectively) of the samples fall within the AOD EE. Although the AE has significant heterogeneity with those values obtained by AERONET ($R^2 = 0.18$, MAE = 0.35, RMSE = 0.48), nearly 2/3 of the samples are still within the EE of AE, which is attributed to the high accuracy of the spectral AOD predictions.

In addition, according to the site based 10-CV, model still demonstrates good spatial prediction capability for spectral AOD (with R^2 of 0.67 and 0.64, respectively). Compared to sample based 10-CV, MAE (0.14 and 0.09, respectively) and RMSE (0.21 and 0.13, respectively) are relatively large, but the growth is basically within 0.05 and still >50% of the independent samples fell with the EE (53% and 61%, respectively). The accuracy of AE decreased significantly ($R^2 = 0.09$, MAE = 0.41, RMSE = 0.54), but still 59% of the data fall within the expected error.

4.2.3. Seasonal performance

Fig. 6 shows the density scatterplots of the sample-based 10CV in different seasons (divided by the Northern Hemisphere seasons, MAM for spring, JJA for summer, SON for autumn and DJF for winter). The accuracy remains high in all seasons. The better retrievals for spectral AOD occurs in MAM and DJF, with $R^2 \geq 0.82$, MAE ≤ 0.11, RMSE ≤ 0.17, and at least 70% of the samples fall within the EE. The correlation coefficient for AE can be as high as 0.19 and 0.17 in MAM and DJF, with MAE ≤ 0.34 and RMSE ≤ 0.47, and >70% of the samples fall within the EE. The accuracy in JJA and SON is decreased, but still shows

comparable accuracy on spectral AOD ($R^2 \geq 0.71$, MAE ≤ 0.09, RMSE ≤ 0.15, EE ≥ 69%) and AE ($R^2 \geq 0.08$, MAE ≤ 0.40, RMSE ≤ 0.52, EE ≥ 60%).

The site based 10-CV validation also follows the seasonal variations (Fig. 7). It is not difficult to find that the summer and autumn AOD has lower accuracy in both tests, and the AE calculated by the spectral values also exhibits the highest biases. This may be related to the complex aerosol hygroscopic growth caused by high relative humidity and frequent precipitation. In contrast, there is a clear improvement for MAM and DJF retrievals, with the AOD $R^2 \geq 0.70$ and ≥ 0.60, respectively. Some AE improvement can be found in these seasons corresponding to the high-quality AOD (both MAE and RMSE are smaller than those in JJA and SON, and over 60% of samples fall within the EE). It is worth noting that the DORF model has a very good performance during the Northern Hemisphere spring and winter, when the atmosphere is exposed to high concentrations of aerosols and multiple anthropogenic pollutants (Song et al., 2008). The good metrics for both AOD and AE imply the prospect of the DORF method applied in high concentration and complex aerosol monitoring.

4.2.4. Hourly performance

Geostationary satellites have the capacity to obtain ultrahigh temporal resolution observations. It is thus also necessary to analyze the hourly accuracy of the model. Fig. 8 shows the performance of sample based 10-CV and site based 10-CV under different hours of the day. The AOD metrics from sample based 10-CV do not significantly suffer from

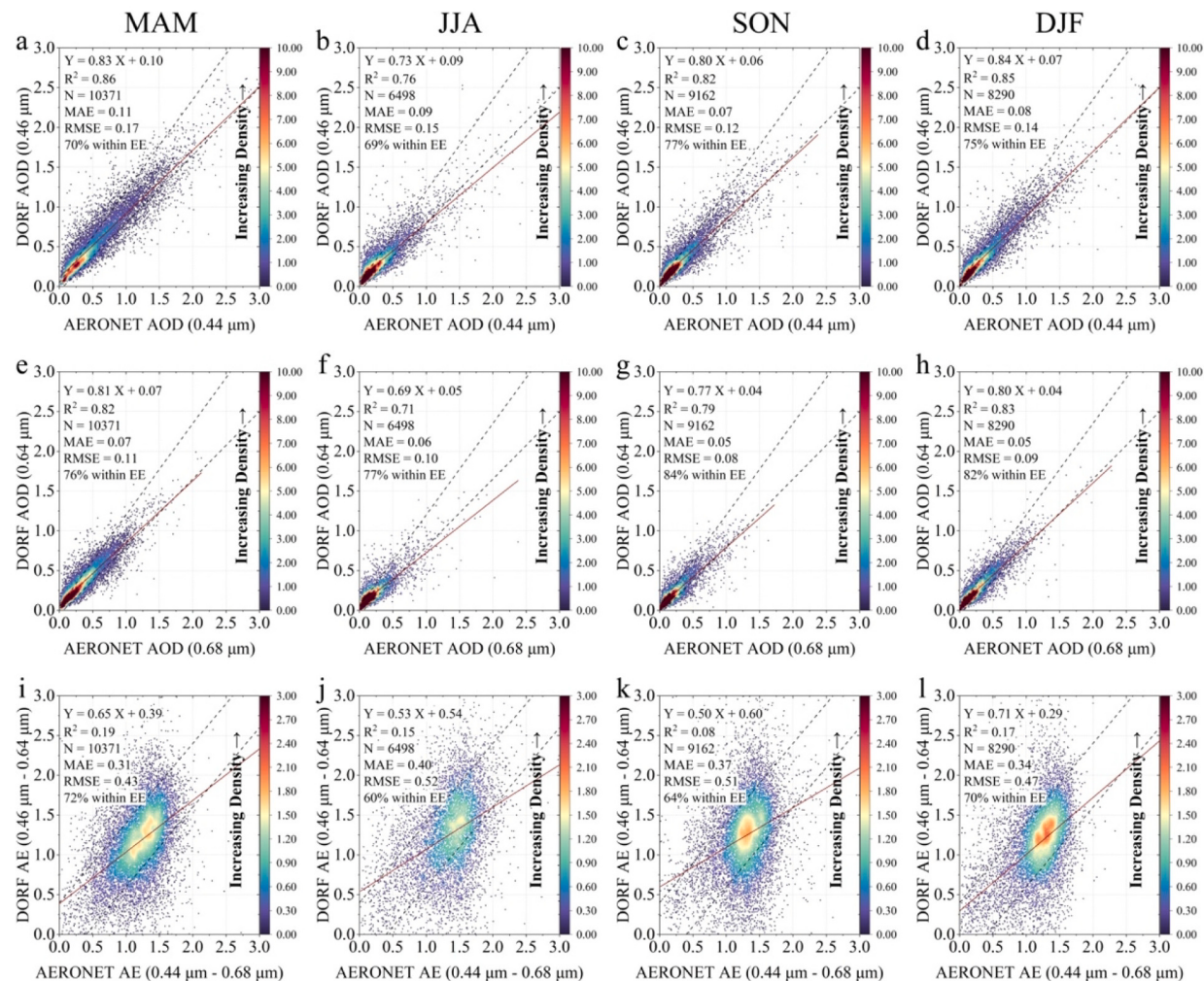


Fig. 6. Density scatterplots of sample based 10-CV for (a, e, i) MAM, (b, f, j) JJA, (c, g, k) SON and (d, h, l) DJF.

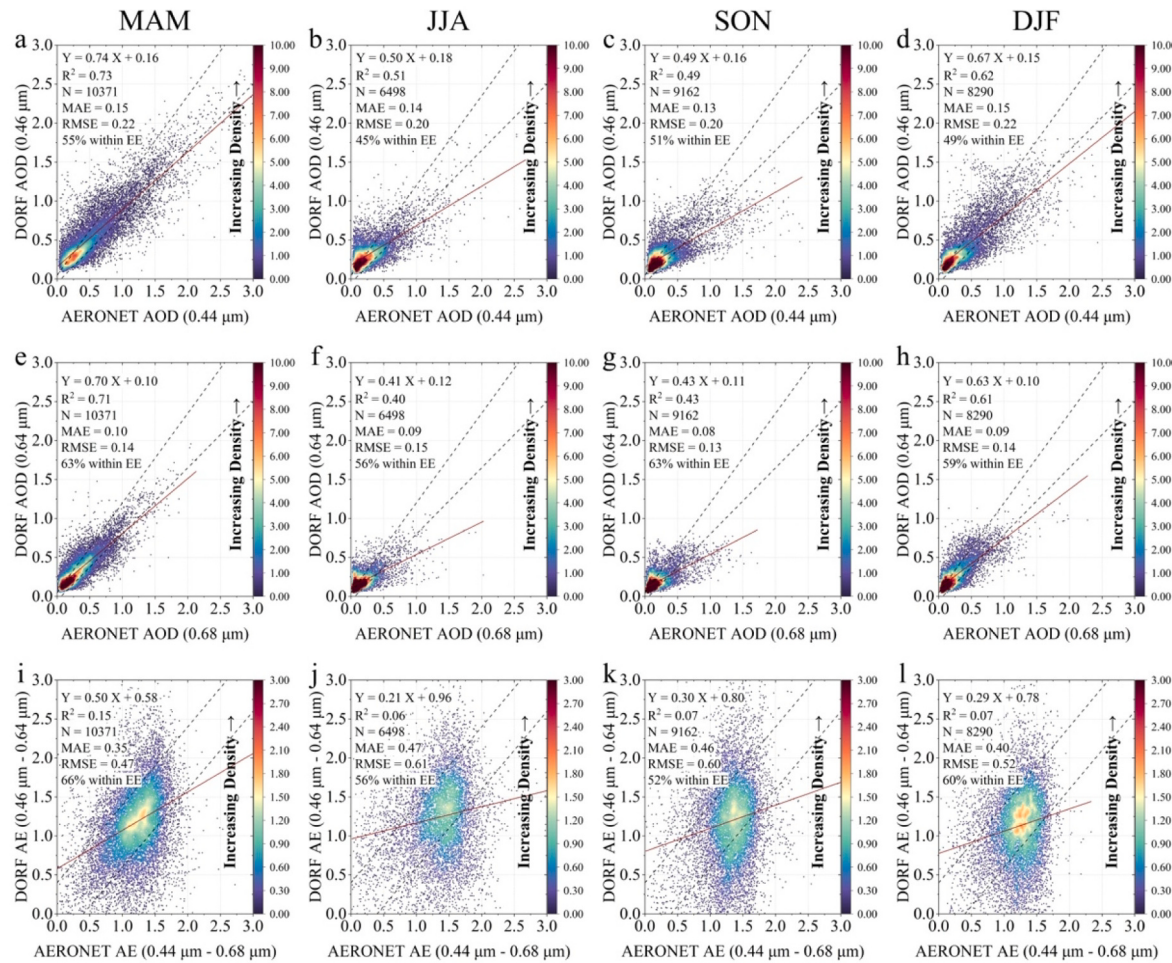


Fig. 7. Same as Fig. 6 but for site based 10-CV.

time-dependent error introduced by the observational geometries. The metrics for AOD at both wavelengths exhibit a time-dependent drop between 22:00 and 00:00, after which the accuracy remains high, with $R^2 \approx 0.80$. These biases may be related to the small amount of data used for modeling and training, making it difficult to acquire enough samples to achieve stable metrics. The AE retrievals is still reliable ($MAE \leq 0.40$, $RMSE \leq 0.50$ and $EE \geq 60\%$) but exhibit more pronounced time-dependent fluctuations. The site based 10-CV test is basically consistent with the sample-based results. The R^2 of AOD can be resolved at about 0.6 after 00:00 UTC, with $MAE \leq 0.15$, $RMSE \leq 0.23$ and more than half of the retrievals fall within EE. AE retrievals from site-based performance does not degrade much, with $EE \approx 60\%$ at all selected daily hours.

4.2.5. Performance in different aerosol types

Prior knowledge of aerosol microphysical properties for different regions is used as a input in the DORF model, which leads to spatial differences in the metrics. Table 2-4 summarize the DORF sampled-based and site-based 10-CV test metrics under different aerosol types. Some models performed extraordinarily well in both tests, such as types 'Agriculture2', 'Urban1' and 'Urban3', which represent aerosol pollution in East Asia and biomass burning in South Asia. The model can capture the temporal and spatial variations of the complex pollution. Additionally, a reduction in samples is more susceptible to greater volatility in accuracy. There is a possibility that predictions may not occur during the training process, and this feature will be further evident in the 10-CV tests. For example, types such as 'AUS1', 'Dust' and 'Forest' have insufficient training samples that exhibit the lower metrics in the

10-CV test. Although the algorithm does not separate land and ocean surfaces, the oceanic retrievals (type 'Marine') exhibit better performance compared to the average metrics of other continental retrievals, which is consistent with some mature physical models.

4.2.6. Site-scaled performance

Figs. 9–10 show the sample-based and site-based 10-CV metrics for each site, further refining the analyses of the accuracy of the spatial heterogeneity. For the sample-based test, >70% of the AERONET sites have AOD correlation coefficients >0.70 at both wavelengths, which shows very small MAEs (averaged 0.09 and 0.06 for 0.46 μm and 0.64 μm AOD, respectively) and RMSEs (averaged 0.14 and 0.09 for 0.46 μm and 0.64 μm AOD, respectively), as well as large fractions within EE (> 70%). The AE results corresponding to these high-quality sites are also very reliable (averaged $R^2 = 0.25$, $MAE = 0.37$, $RMSE = 0.49$, $EE = 66\%$).

It can be seen from the site based 10-CV spatial patterns that approximately 2/3 of the sites still exhibit reasonable AOD estimates, with $R^2 \geq 0.60$. Better spatial predictions can be found in Southern Asia and Eastern Asia, where dense sites are distributed. This result supports that the DORF model is excellent for aerosol estimation in regions with dense human activities and high pollutant emissions. The AE metrics corresponding to these samples may exhibit ambiguity with larger biases, but 2/3 of the stations are still shows reasonable fractions within EE ($\geq 50\%$).

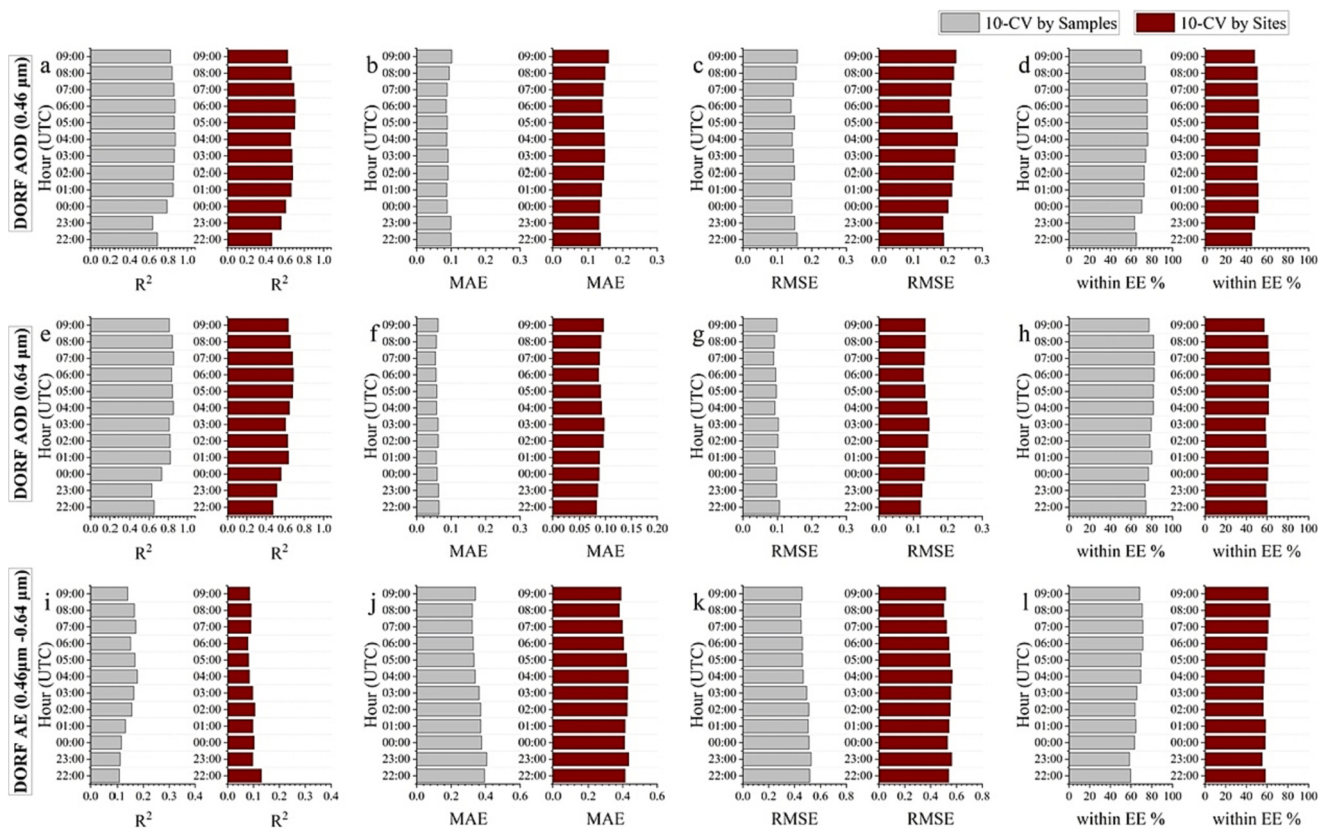


Fig. 8. The metrics of the DORF sample based and site based 10-CV test for different daily hours. (a-d) AOD at 0.46 μm . (e-h) AOD at 0.64 μm . (i-l) AE calculated by spectral AODs.

Table 2
Sampled-based and site-based 10-CV under different aerosol models – AOD at 0.46 μm .

Type	N	Sample-Based 10-CV				Site-Based 10-CV			
		R ²	MAE	RMSE	EE	R ²	MAE	RMSE	EE
Agriculture1	5089	0.71	0.09	0.15	66%	0.63	0.16	0.24	48%
Agriculture2	9306	0.84	0.12	0.18	73%	0.67	0.20	0.29	46%
Dust	849	0.46	0.03	0.07	90%	0.33	0.10	0.17	54%
Forest	656	0.49	0.05	0.08	83%	0.37	0.14	0.21	52%
Urban1	1398	0.92	0.09	0.15	81%	0.89	0.10	0.18	79%
Urban2	3811	0.65	0.13	0.19	58%	0.43	0.17	0.23	44%
Urban3	9929	0.78	0.08	0.12	72%	0.71	0.10	0.14	61%
AUS1	129	0.68	0.03	0.04	93%	0.52	0.12	0.19	51%
AUS2	2135	0.71	0.03	0.06	93%	0.58	0.12	0.18	55%
Marine	1019	0.76	0.05	0.08	83%	0.61	0.13	0.20	56%
Continental Averaged		0.69	0.07	0.12	79%	0.57	0.13	0.20	54%

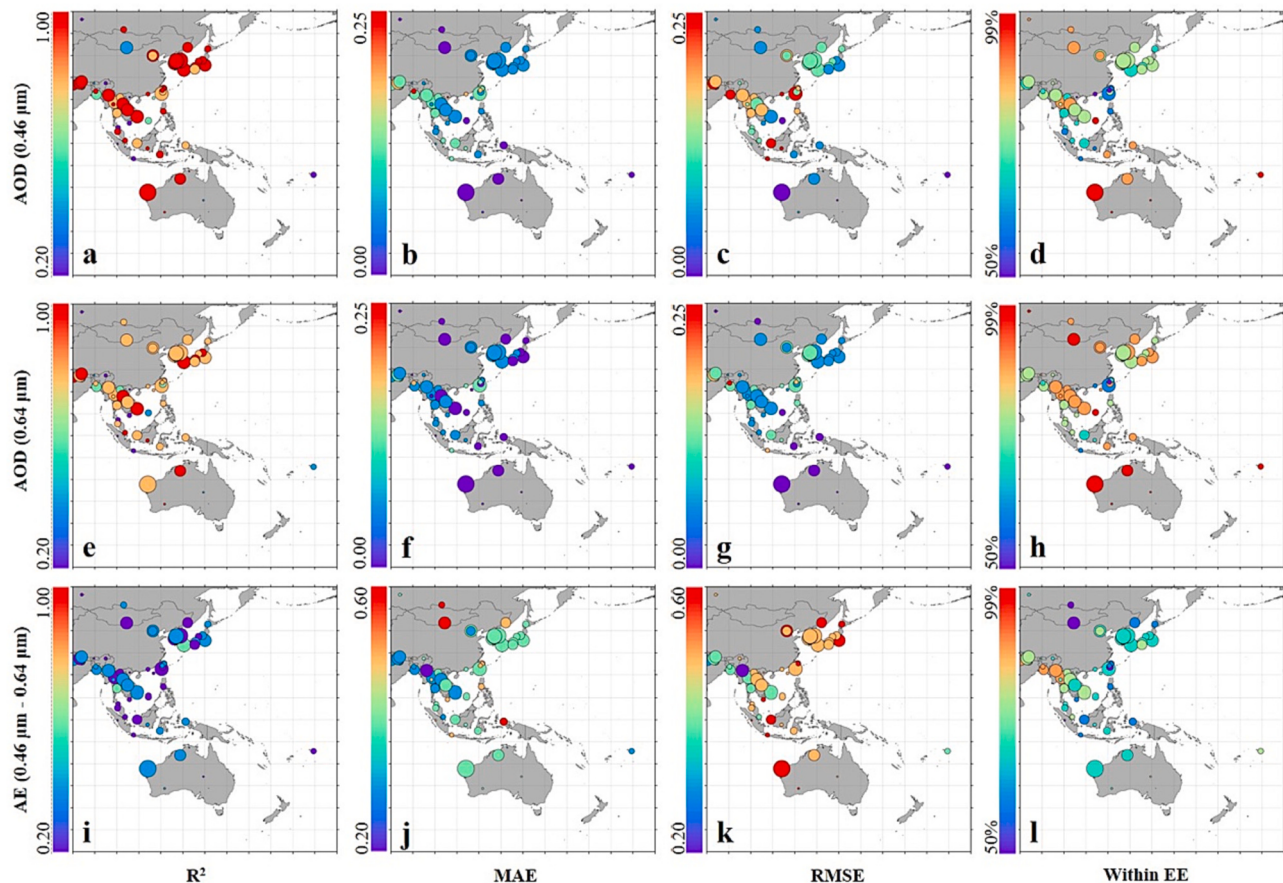
Table 3
Sampled-based and site-based 10-CV under different aerosol models – AOD at 0.64 μm .

Type	N	Sample-Based 10-CV				Site-Based 10-CV			
		R ²	MAE	RMSE	EE	R ²	MAE	RMSE	EE
Agriculture1	5089	0.65	0.06	0.09	75%	0.58	0.11	0.14	58%
Agriculture2	9306	0.82	0.07	0.11	80%	0.65	0.12	0.17	56%
Dust	849	0.42	0.03	0.06	90%	0.31	0.1	0.15	58%
Forest	656	0.42	0.03	0.05	90%	0.32	0.08	0.13	60%
Urban1	1398	0.91	0.06	0.10	85%	0.85	0.07	0.13	82%
Urban2	3811	0.57	0.09	0.13	64%	0.36	0.11	0.16	52%
Urban3	9929	0.75	0.05	0.08	80%	0.66	0.06	0.10	72%
AUS1	129	0.41	0.02	0.03	94%	0.29	0.08	0.15	56%
AUS2	2135	0.73	0.02	0.03	97%	0.59	0.08	0.09	61%
Marine	1019	0.74	0.03	0.05	90%	0.64	0.07	0.13	64%
Continental Averaged		0.63	0.05	0.08	83%	0.51	0.09	0.14	62%

Table 4

Sampled-based and site-based 10-CV under different aerosol models– AE.

Type	N	Sample-Based 10-CV				Site-Based 10-CV			
		R ²	MAE	RMSE	EE	R ²	MAE	RMSE	EE
Agriculture1	5089	0.07	0.36	0.48	65%	0.03	0.43	0.54	58%
Agriculture2	9306	0.18	0.21	0.36	80%	0.07	0.35	0.46	63%
Dust	849	0.04	0.48	0.65	50%	0.01	0.55	0.71	45%
Forest	656	0.04	0.46	0.62	54%	0.01	0.50	0.64	50%
Urban1	1398	0.35	0.22	0.33	83%	0.23	0.29	0.45	74%
Urban2	3811	0.06	0.38	0.51	63%	0.02	0.35	0.47	62%
Urban3	9929	0.15	0.33	0.45	68%	0.06	0.38	0.50	60%
AUS1	129	0.12	0.37	0.55	68%	0.05	0.45	0.64	53%
AUS2	2135	0.26	0.35	0.49	67%	0.09	0.41	0.53	57%
Marine	1019	0.21	0.31	0.42	70%	0.11	0.37	0.47	65%
Continental Averaged		0.14	0.35	0.49	67%	0.06	0.41	0.55	58%

**Fig. 9.** The metrics of the DORF sample based 10-CV metrics over different AERONET sites. (a-d) AOD at 0.46 μm . (e-h) AOD at 0.64 μm . (i-l) AE calculated by spectral AODs.

4.3. Comparison with other models

4.3.1. Overall accuracy against the Himawari-8 operational aerosol products

To demonstrate the advantages of machine learning algorithms, Himawari-8 operational L2 Aerosol Properties (L2ARP) products is used for comparison. Fig. 11(a-b) illustrates an overall evaluation of Himawari-8 L2ARP, including AOD at 0.50 μm ($R^2 = 0.52$, MAE = 0.17, RMSE = 0.26, EE = 45%) and AE ($R^2 = 0.01$, MAE = 0.45, RMSE = 0.56, EE = 52%). Significant improvements can be recognized via sample based 10-CV validation of DORF model (Fig. 11c), with approximately 50% improvement on AOD retrievals ($R^2 = 0.85$, MAE = 0.08, RMSE = 0.13, EE = 76%) and 20% improvement on AE retrievals ($R^2 = 0.18$, MAE = 0.35, RMSE = 0.48, EE = 67%, see Fig. 5f). Although the site-

based performance decreases (Fig. 11d), they still show a 30% improvement on AOD, with R^2 of 0.67, MAE of 0.12, RMSE of 0.18, and EE of 57%. The site-based AE retrievals (see Fig. 5i) also show an improvement beyond 10% (MAE = 0.41, RMSE = 0.54), with higher correlation coefficients ($R^2 = 0.09$) and more samples falling within the EE (59%).

4.3.2. Comparisons with other Himawari-8 machine learning models

Table 5 summarizes the comparison between the DORF model and other learning/deep learning models, focusing on aerosol retrievals directly from Himawari-8 TOA measurements. Three different references is selected based on their study area and strategy, including origin RF model for AOD (She et al., 2020), mature algorithm corrected by deep learning approach (Su et al., 2020), and NN approach for AOD and

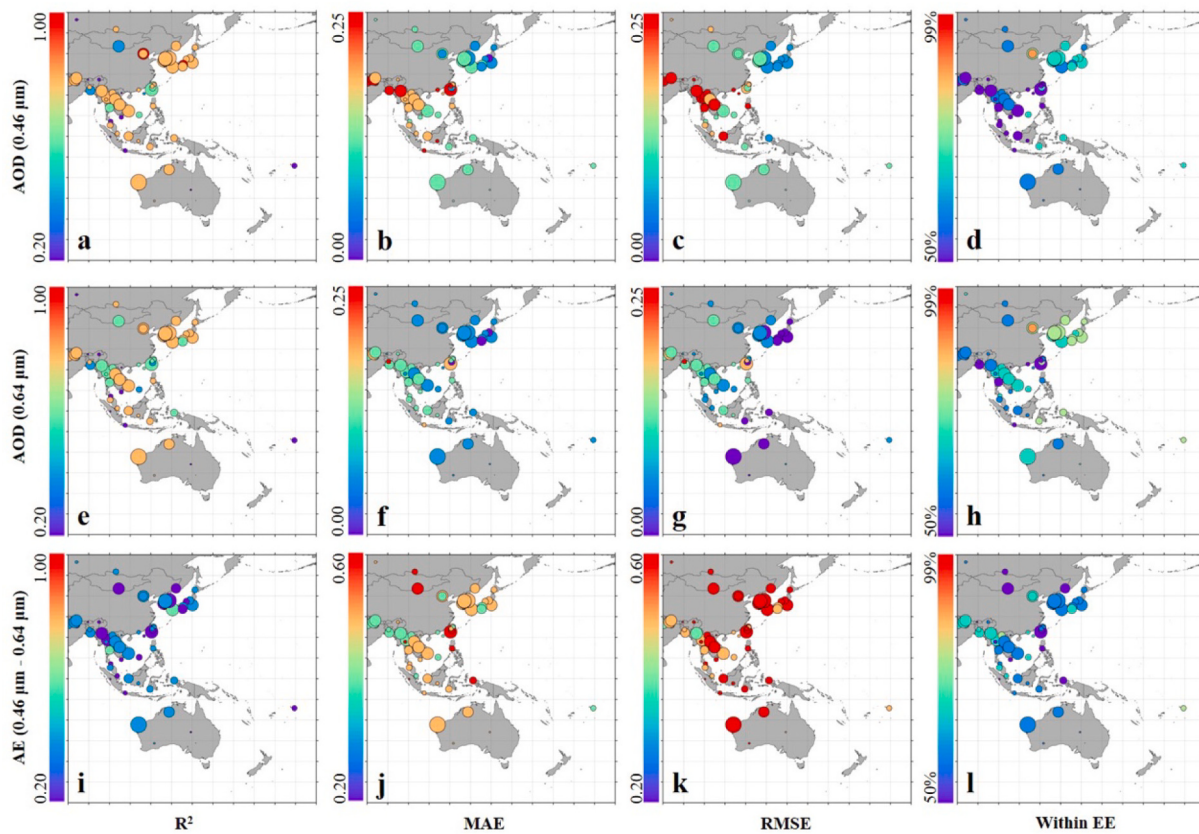


Fig. 10. Same as Fig. 9 but for site based 10-CV.

AE (Chen et al., 2022b). Note that the performance of DORF model will be evaluated using the same AERONET sites and validation approaches of the references, which were inconsistent across studies.

Compared to the origin RF method, the DORF model has no significant improvement in AOD ($0.50 \mu\text{m}$) retrieval over the whole AHI domain. The significant improvement is the higher slope of the linear fit in the validation, which indicates a weaker underestimation of AOD under hazy conditions. However, the DORF model exhibits good capability over specific areas. For example, compared to the coupled Deep neural network (DNN) and physical model over Southern Asia ($R^2 = 0.74$, $\text{MAE} = 0.14$, $\text{RMSE} = 0.09$), DORF model shows a better performance on AOD retrieval, with R^2 of 0.79, MAE of 0.07 and RMSE of 0.11. Another improvement is that DORF model tries to obtain the spectral information of aerosols through independent TOA reflectance, rather than focusing on the AOD at a particular band through multiple TOA reflectance. These spectral AOD retrievals is useful for subsequent aerosol type determination. It can be proved from the comparison over China, which shows that the metrics of the DORF aerosol retrievals are comparable to those of complex NN models, but exhibits specific improvement on AE. Higher R^2 also indicates a more accurate description of regional aerosol type differences.

4.4. Hourly scale aerosol monitoring from DORF

Figs. 12-13 show two different pollution cases, including biomass burning in southern Asia (March 2nd, 2018) and urban agglomeration pollution in eastern Asia (October 4th, 2018), where DORF exhibits good performance. The hourly patterns of AOD and AE are all generated by the DORF model at 5 km resolution scales. Here, AOD patterns at $0.50 \mu\text{m}$ wavelength are calculated from the two spectral AODs ($0.46 \mu\text{m}$ and $0.64 \mu\text{m}$) and their AE values. The corresponding level 2 operational AHI aerosol products (L2 ARP) are presented in Appendix Figs. A4-A5. It

should be noted that small AE values ($\alpha \leq 1$) indicate size distributions dominated by coarse mode aerosols that are typically associated with dust and sea salt, and values of $\alpha \geq 1$ indicate size distributions dominated by fine mode aerosols (e.g., urban pollution and biomass burning).

The Indo-Gangetic Plain is a region of extensive biomass burning activities, and biomass burning aerosols are typically generated in the upper Ganges and transported eastward with the summer monsoon. These aerosols are the blocked by Himalayan Mountains, which results in aerosol accumulation in Bengal Bay (Ramanathan and Ramana, 2005). Since the region is located at the edge of the AHI domain ($80^\circ \text{E} - 100^\circ \text{E}$), Case 1 is able to test the aerosol monitoring capability of the DORF model at large observation and solar angles. The AOD patterns show that the DORF model is good at depicting spatial detail and temporal variation, which is consistent with the AERONET observations. Biomass burning aerosols, mainly consisting of fine particles, can be identified by the DORF AE patterns. The spatial coverage is more complete compared to the operational product, especially under large geometries (02:00 UTC-04:00 UTC). This is related to the better performance of the DORF model with lower time-dependent error introduced by the geometries.

It is widely reported that urban agglomeration aerosols produced by industrial and anthropogenic activities are the main aerosol features in Eastern Asia. Case 2 has been confirmed by our previous studies to be a typical case of strong absorptive aerosol pollution, with high concentrations of carbonaceous aerosols observed (including elemental carbon and organic carbon) (Gao et al., 2022; Gao et al., 2020). The simulations of the DORF model demonstrate the complete spatial distribution of aerosol properties and the smoothing of developmental changes in pollution. Compared to the L2 ARP AHI aerosol products, the AE results operated by the DORF model are also able to better distinguish the main characteristics of fine mode aerosols from coarse mode aerosols associated with dust, with smoother intraday variations without significant

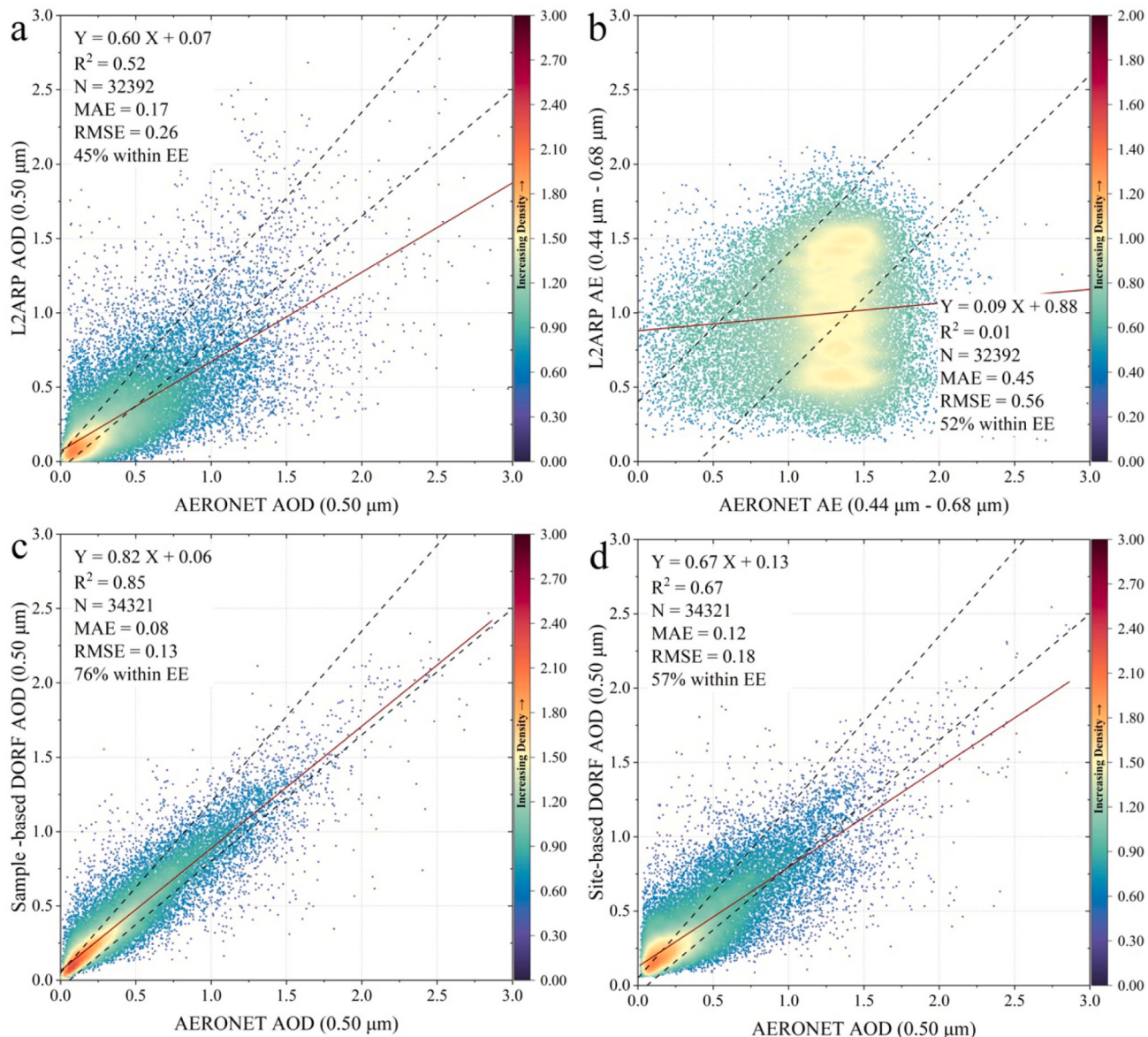


Fig. 11. Density scatterplots of (a) Himawari-8 L2 ARP AOD at 0.50 μm , (b) Himawari-8 L2 ARP AE at 0.46 μm –0.68 μm , (c) DORF Sample-based 10-CV AOD at 0.50 μm , and (d) DORF Site-based 10-CV AOD at 0.50 μm against AERONET truth. The sample-based and site-based 10-CV AE can be found in Fig. 5f and Fig. 5i, respectively.

Table 5
Summaries of the comparison between the DORF model and other models for AHI aerosol properties retrievals.

Ref.	Model	Study Area	Validation Method	AOD at 0.5 μm	AE	DORF AOD	DORF AE
She et al. (2020)	Original RF	Whole AHI Domain	76-fold CV by samples	R ² = 0.86 RMSE = 0.12 $y = 0.77x + 0.07$	/	R ² = 0.85 RMSE = 0.13 $y = 0.82x + 0.06$	/
			Leave one station out validation	R ² = 0.67 RMSE = 0.19 $y = 0.55x + 0.16$	/	R ² = 0.67 RMSE = 0.18 $y = 0.67x + 0.13$	/
Su et al. (2020)	DNN + Physical	Southern Asia	Normal validation	R ² = 0.74 RMSE = 0.14 MAE = 0.09	/	R ² = 0.79 RMSE = 0.11 MAE = 0.07	/
Chen et al. (2022b)	NN	China	75%Modeling +25% Validation	R ² = 0.86 RMSE = 0.12 MAE = 0.09 Within EE = 64%	R ² = 0.08 RMSE = 0.31 MAE = 0.24 Within EE =	R ² = 0.85 RMSE = 0.14 MAE = 0.09 Within EE = 71%	R ² = 0.23 RMSE = 0.39 MAE = 0.28 Within EE = 58%

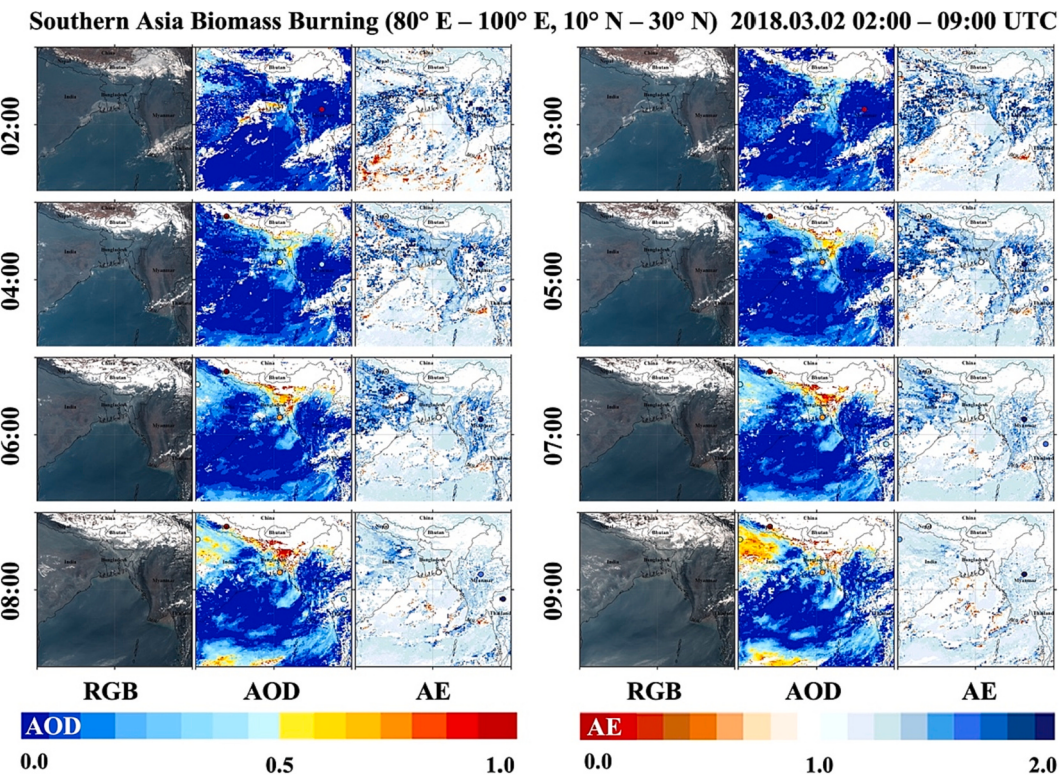


Fig. 12. Biomass burning (March 2nd, 2018) in southern Asia (80° E - 100° E, 10° N - 30° N) based on hourly (02:00 UTC – 09:00 UTC) DORF model aerosol inversions overlayed by AERONET observations. From left to right are the RGB image of AHI, AOD patterns at $0.50\text{ }\mu\text{m}$ calculated by spectral AODs and their AE patterns, respectively.

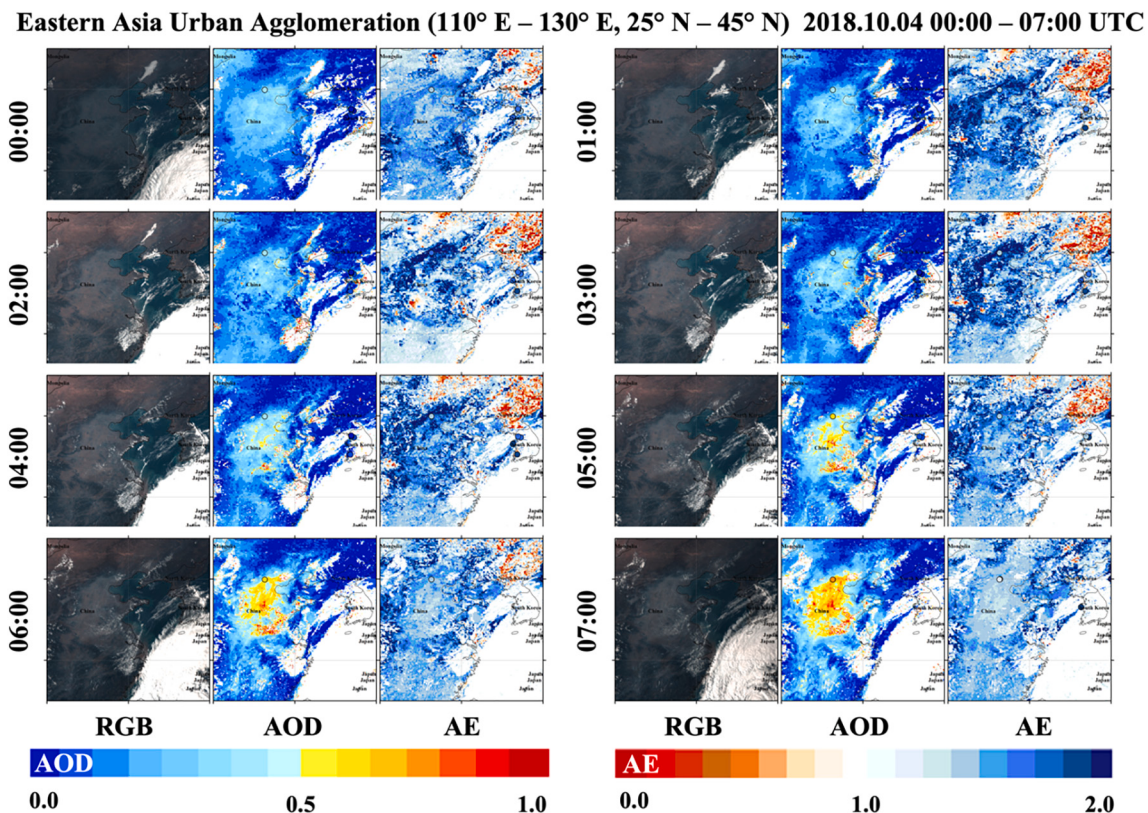


Fig. 13. Same as Fig. 12 but for urban agglomeration pollution (October 4th, 2018, 00:00 UTC – 07:00 UTC) in Eastern Asia (110° E - 130° E, 25° N – 45° N).

fluctuations.

5. Conclusion

Applying machine learning models to satellite aerosol remote sensing is a popular focus in current quantitative remote sensing research, with the goals of addressing the issues of current traditional physical retrieval models and improving retrieval efficiency and accuracy. Some relevant studies have achieved high levels in aerosol retrieval but still lack analyses of key features variables and their importance measures that would help estimate the strength of the relationship between aerosol parameters and features. In addition, some machine learning models usually retrieves one parameter from multiple band synthesis, and thus the spectral AODs and relevant AE retrievals is missing, which is inconsistent with the mature physical algorithms.

To address these challenges, a key feature for geostationary satellite aerosol retrieval is developed based on the radiative transfer equation, which quantifies the simple linear relationship of AOD on TOA reflectance enhancement. The operator can greatly simplify the ground-aerosol decoupling issues and effectively reducing the uncertainties. Additionally, this approach substantially reduces the effect of slow-change parameters, such as surfaces and meteorological parameters, while also offering mathematical simplicity and maintaining physical coherency within the model. Based on the analyses of key feature inputs and important measures, a random forest model based on differential operator for AOD acquisition and further AE calculations is developed. The model performance is evaluated using a series of comprehensive temporal and spatial validation analyses, with reference to the widely used physical and machine learning models. The results show that the DORF model can significantly improve the estimation of aerosol properties using Himawari AHI geostationary observations. Two typical regional pollution cases also highlight the advantages of the DORF model for aerosol monitoring. Aerosol patterns with 5 km resolution exhibit a very good spatial coverage and accuracy on polluted plumes even for large observations and solar angles. The aerosol results have smoother intraday variability and offer good performance in the characterization of pollution types, such as distinguishing coarse mode aerosols associated with dust from fine-mode aerosols associated with

the burning of biomass.

These results demonstrate that the DORF model and its products are useful in air quality studies. The acquisition of aerosol properties by the DORF model is easily processed, flexible, and accurate. It can simultaneously and rapidly obtain high-level hourly aerosol properties from Himawari geostationary satellite observations without excessive auxiliary parameters, which provides a new prospective for machine learning applications in aerosol remote sensing. For future work, a higher resolution strategy (with a spatial resolution of 1 km and a temporal resolution of 10 min) is expected to improve the performance of DORF products while also attempting to obtain more aerosol information by using other implied features related to aerosol radiative transfer.

CRediT authorship contribution statement

Fangwen Bao: Conceptualization, Methodology, Writing – review & editing. **Kai Huang:** Data curation, Software, Visualization. **Shengbiao Wu:** Investigation, Validation.

Declaration of Competing Interest

The authors declare that they have no known competing financial interests or personal relationships that could have appeared to influence the work reported in this paper.

Data availability

No data was used for the research described in the article.

Acknowledgment

This research was funded by the National Natural Science Foundation of China, grant number 42105124; Guangdong Basic and Applied Basic Research Fund Committee (2019A1515110384). The authors would like to thank the JAXA for providing access to the Himawari products. The authors would like to thank the PHOTONS group of Laboratoire d'Optique Atmosphérique, University Lille 1, France, for their work of AERONET.

Appendix A. Appendix

Table A1
Clustered aerosols models- real part of refractive indexes (RIR).

	Percentage*	440 nm	675 nm	870 nm	1020 nm
Agriculture1					
MAM	35.3%	1.39 ± 0.05	1.41 ± 0.04	1.42 ± 0.04	1.43 ± 0.04
JJA	40.0%	1.44 ± 0.05	1.45 ± 0.04	1.45 ± 0.04	1.45 ± 0.04
SON	52.8%	1.44 ± 0.05	1.45 ± 0.04	1.46 ± 0.04	1.46 ± 0.04
DJF	43.8%	1.41 ± 0.06	1.43 ± 0.05	1.44 ± 0.04	1.44 ± 0.04
Agriculture2					
MAM	35.6%	1.46 ± 0.05	1.49 ± 0.05	1.50 ± 0.05	1.50 ± 0.05
JJA	45.7%	1.48 ± 0.06	1.50 ± 0.06	1.50 ± 0.05	1.50 ± 0.05
SON	43.4%	1.44 ± 0.06	1.46 ± 0.06	1.47 ± 0.05	1.46 ± 0.05
DJF	37.3%	1.45 ± 0.06	1.46 ± 0.05	1.47 ± 0.05	1.46 ± 0.04
Dust	54.4%	1.49 ± 0.04	1.51 ± 0.04	1.50 ± 0.04	1.49 ± 0.04
Forest	37.1%	1.48 ± 0.05	1.49 ± 0.04	1.50 ± 0.04	1.50 ± 0.04
Marine	38.2%	1.43 ± 0.05	1.44 ± 0.04	1.44 ± 0.04	1.44 ± 0.04
Urban1					
MAM	39.6%	1.48 ± 0.05	1.51 ± 0.05	1.51 ± 0.04	1.50 ± 0.04
JJA	34.7%	1.44 ± 0.04	1.44 ± 0.04	1.44 ± 0.04	1.43 ± 0.04
SON	31.6%	1.45 ± 0.06	1.46 ± 0.05	1.46 ± 0.05	1.46 ± 0.05
DJF	29.8%	1.47 ± 0.06	1.49 ± 0.05	1.49 ± 0.05	1.48 ± 0.04
Urban2					
MAM	34.8%	1.43 ± 0.04	1.43 ± 0.04	1.43 ± 0.04	1.43 ± 0.04
JJA	46.0%	1.39 ± 0.03	1.39 ± 0.03	1.40 ± 0.03	1.39 ± 0.03
SON	60.0%	1.41 ± 0.04	1.41 ± 0.03	1.42 ± 0.03	1.41 ± 0.03
DJF	36.8%	1.42 ± 0.04	1.43 ± 0.03	1.43 ± 0.03	1.43 ± 0.03

(continued on next page)

Table A1 (continued)

	Percentage*	440 nm	675 nm	870 nm	1020 nm
Urban3					
MAM	37.1%	1.46 ± 0.06	1.48 ± 0.05	1.48 ± 0.04	1.48 ± 0.04
JJA	58.9%	1.41 ± 0.05	1.42 ± 0.04	1.42 ± 0.04	1.42 ± 0.04
SON	41.5%	1.43 ± 0.06	1.44 ± 0.05	1.44 ± 0.04	1.44 ± 0.04
DJF	42.6%	1.44 ± 0.06	1.46 ± 0.04	1.47 ± 0.04	1.46 ± 0.04
AUS1	51.7%	1.48 ± 0.08	1.50 ± 0.07	1.51 ± 0.06	1.50 ± 0.06
AUS2	23.4%	1.45 ± 0.07	1.47 ± 0.05	1.47 ± 0.05	1.47 ± 0.04

* Note: Percentage of Aerosols in all clustered results.

Table A2

Clustered aerosols models - imaginary part of refractive indexes (RII).

	440 nm	675 nm	870 nm	1020 nm
Agriculture1				
MAM	0.004 ± 0.002	0.003 ± 0.001	0.003 ± 0.001	0.003 ± 0.002
JJA	0.003 ± 0.001	0.002 ± 0.001	0.002 ± 0.001	0.002 ± 0.001
SON	0.003 ± 0.001	0.003 ± 0.001	0.003 ± 0.001	0.003 ± 0.002
DJF	0.005 ± 0.003	0.004 ± 0.002	0.003 ± 0.002	0.003 ± 0.002
Agriculture2				
MAM	0.006 ± 0.002	0.004 ± 0.001	0.003 ± 0.001	0.003 ± 0.001
JJA	0.003 ± 0.001	0.002 ± 0.001	0.001 ± 0.001	0.002 ± 0.001
SON	0.007 ± 0.003	0.005 ± 0.002	0.005 ± 0.002	0.004 ± 0.002
DJF	0.010 ± 0.003	0.007 ± 0.002	0.008 ± 0.002	0.008 ± 0.002
Dust	0.005 ± 0.002	0.002 ± 0.001	0.002 ± 0.002	0.003 ± 0.002
Forest	0.004 ± 0.001	0.003 ± 0.001	0.003 ± 0.001	0.003 ± 0.001
Marine	0.002 ± 0.001	0.002 ± 0.001	0.002 ± 0.001	0.002 ± 0.001
Urban1				
MAM	0.005 ± 0.002	0.002 ± 0.001	0.002 ± 0.001	0.002 ± 0.001
JJA	0.003 ± 0.001	0.002 ± 0.001	0.002 ± 0.001	0.002 ± 0.001
SON	0.005 ± 0.002	0.003 ± 0.001	0.003 ± 0.001	0.003 ± 0.001
DJF	0.008 ± 0.003	0.004 ± 0.001	0.004 ± 0.001	0.004 ± 0.002
Urban2				
MAM	0.003 ± 0.002	0.002 ± 0.001	0.002 ± 0.001	0.002 ± 0.001
JJA	0.002 ± 0.001	0.002 ± 0.001	0.002 ± 0.001	0.002 ± 0.001
SON	0.002 ± 0.001	0.002 ± 0.001	0.002 ± 0.001	0.002 ± 0.001
DJF	0.002 ± 0.001	0.002 ± 0.001	0.002 ± 0.001	0.002 ± 0.001
Urban3				
MAM	0.003 ± 0.002	0.002 ± 0.001	0.002 ± 0.001	0.002 ± 0.001
JJA	0.003 ± 0.001	0.002 ± 0.001	0.002 ± 0.001	0.002 ± 0.001
SON	0.004 ± 0.002	0.003 ± 0.001	0.003 ± 0.001	0.003 ± 0.002
DJF	0.004 ± 0.002	0.003 ± 0.001	0.003 ± 0.001	0.003 ± 0.002
AUS1	0.004 ± 0.002	0.002 ± 0.001	0.002 ± 0.001	0.002 ± 0.001
AUS2	0.009 ± 0.003	0.007 ± 0.003	0.007 ± 0.003	0.007 ± 0.003

Table A3

Clustered aerosols models - single scattering albedo (SSA).

	440 nm	675 nm	870 nm	1020 nm
Agriculture1				
MAM	0.96 ± 0.02	0.96 ± 0.02	0.96 ± 0.02	0.95 ± 0.02
JJA	0.98 ± 0.01	0.98 ± 0.01	0.97 ± 0.01	0.97 ± 0.02
SON	0.98 ± 0.01	0.98 ± 0.01	0.97 ± 0.01	0.97 ± 0.02
DJF	0.95 ± 0.02	0.96 ± 0.02	0.96 ± 0.02	0.95 ± 0.02
Agriculture2				
MAM	0.91 ± 0.04	0.94 ± 0.02	0.94 ± 0.02	0.95 ± 0.02
JJA	0.93 ± 0.03	0.97 ± 0.02	0.97 ± 0.01	0.97 ± 0.01
SON	0.94 ± 0.03	0.95 ± 0.02	0.95 ± 0.02	0.94 ± 0.03
DJF	0.92 ± 0.02	0.93 ± 0.02	0.92 ± 0.02	0.91 ± 0.03
Dust	0.91 ± 0.03	0.96 ± 0.02	0.96 ± 0.02	0.96 ± 0.02
Forest	0.97 ± 0.01	0.97 ± 0.01	0.97 ± 0.02	0.97 ± 0.02
Marine	0.98 ± 0.01	0.98 ± 0.01	0.97 ± 0.01	0.97 ± 0.02
Urban1				
MAM	0.92 ± 0.03	0.96 ± 0.02	0.96 ± 0.02	0.97 ± 0.02
JJA	0.97 ± 0.02	0.98 ± 0.01	0.98 ± 0.01	0.97 ± 0.01
SON	0.95 ± 0.03	0.96 ± 0.01	0.96 ± 0.02	0.96 ± 0.02
DJF	0.93 ± 0.03	0.95 ± 0.02	0.95 ± 0.02	0.95 ± 0.02
Urban2				
MAM	0.97 ± 0.01	0.98 ± 0.01	0.97 ± 0.01	0.97 ± 0.02
JJA	0.99 ± 0.01	0.99 ± 0.01	0.98 ± 0.01	0.98 ± 0.01
SON	0.98 ± 0.01	0.98 ± 0.01	0.98 ± 0.01	0.97 ± 0.02

(continued on next page)

Table A3 (continued)

	440 nm	675 nm	870 nm	1020 nm
DJF	0.98 ± 0.01	0.98 ± 0.01	0.98 ± 0.01	0.97 ± 0.01
Urban3				
MAM	0.95 ± 0.03	0.97 ± 0.01	0.97 ± 0.01	0.97 ± 0.01
JJA	0.98 ± 0.01	0.98 ± 0.01	0.97 ± 0.01	0.97 ± 0.02
SON	0.97 ± 0.02	0.97 ± 0.01	0.97 ± 0.02	0.96 ± 0.02
DJF	0.96 ± 0.02	0.97 ± 0.01	0.97 ± 0.02	0.97 ± 0.02
AUS1	0.95 ± 0.04	0.97 ± 0.01	0.97 ± 0.02	0.97 ± 0.02
AUS2	0.91 ± 0.03	0.92 ± 0.03	0.91 ± 0.03	0.90 ± 0.04

Table A4

Clustered aerosols models - volumetric size distribution (VSD)/μm.

	r_m, f	σ_f	r_m, c	σ_c
Agriculture1				
MAM	0.18 ± 0.02	0.46 ± 0.05	2.41 ± 0.45	0.63 ± 0.06
JJA	0.18 ± 0.03	0.48 ± 0.06	2.22 ± 0.44	0.64 ± 0.06
SON	0.20 ± 0.03	0.51 ± 0.05	2.63 ± 0.46	0.63 ± 0.06
DJF	0.18 ± 0.02	0.49 ± 0.07	2.34 ± 0.45	0.63 ± 0.07
Agriculture2				
MAM	0.13 ± 0.03	0.47 ± 0.08	2.22 ± 0.29	0.61 ± 0.05
JJA	0.13 ± 0.04	0.53 ± 0.09	2.11 ± 0.32	0.60 ± 0.06
SON	0.18 ± 0.04	0.47 ± 0.05	2.50 ± 0.42	0.60 ± 0.04
DJF	0.19 ± 0.04	0.50 ± 0.06	2.56 ± 0.38	0.62 ± 0.05
Dust	0.14 ± 0.05	0.61 ± 0.09	2.04 ± 0.38	0.60 ± 0.07
Forest	0.17 ± 0.02	0.48 ± 0.06	2.32 ± 0.49	0.68 ± 0.07
Marine	0.19 ± 0.03	0.49 ± 0.06	2.31 ± 0.41	0.62 ± 0.06
Urban1				
MAM	0.15 ± 0.05	0.52 ± 0.10	2.11 ± 0.34	0.61 ± 0.06
JJA	0.23 ± 0.05	0.52 ± 0.06	2.64 ± 0.33	0.60 ± 0.05
SON	0.20 ± 0.05	0.52 ± 0.06	2.47 ± 0.32	0.61 ± 0.05
DJF	0.18 ± 0.05	0.53 ± 0.06	2.31 ± 0.37	0.62 ± 0.05
Urban2				
MAM	0.20 ± 0.04	0.52 ± 0.05	2.25 ± 0.35	0.61 ± 0.04
JJA	0.22 ± 0.04	0.49 ± 0.04	2.58 ± 0.37	0.59 ± 0.05
SON	0.22 ± 0.04	0.50 ± 0.05	2.48 ± 0.31	0.59 ± 0.05
DJF	0.21 ± 0.04	0.53 ± 0.06	2.45 ± 0.29	0.59 ± 0.05
Urban3				
MAM	0.15 ± 0.04	0.50 ± 0.08	1.96 ± 0.35	0.62 ± 0.05
JJA	0.20 ± 0.04	0.50 ± 0.06	2.47 ± 0.38	0.62 ± 0.05
SON	0.19 ± 0.04	0.49 ± 0.05	2.29 ± 0.31	0.61 ± 0.04
DJF	0.19 ± 0.04	0.53 ± 0.07	2.30 ± 0.37	0.61 ± 0.05
AUS1	0.15 ± 0.03	0.45 ± 0.11	2.23 ± 0.31	0.63 ± 0.05
AUS2	0.14 ± 0.02	0.42 ± 0.08	1.98 ± 0.29	0.69 ± 0.06

r_m and σ is the Median Radius and Geometric Standard Deviation of Lognormal Distribution; Subscripts f and subscripts c represent for the fine and coarse model component respectively.

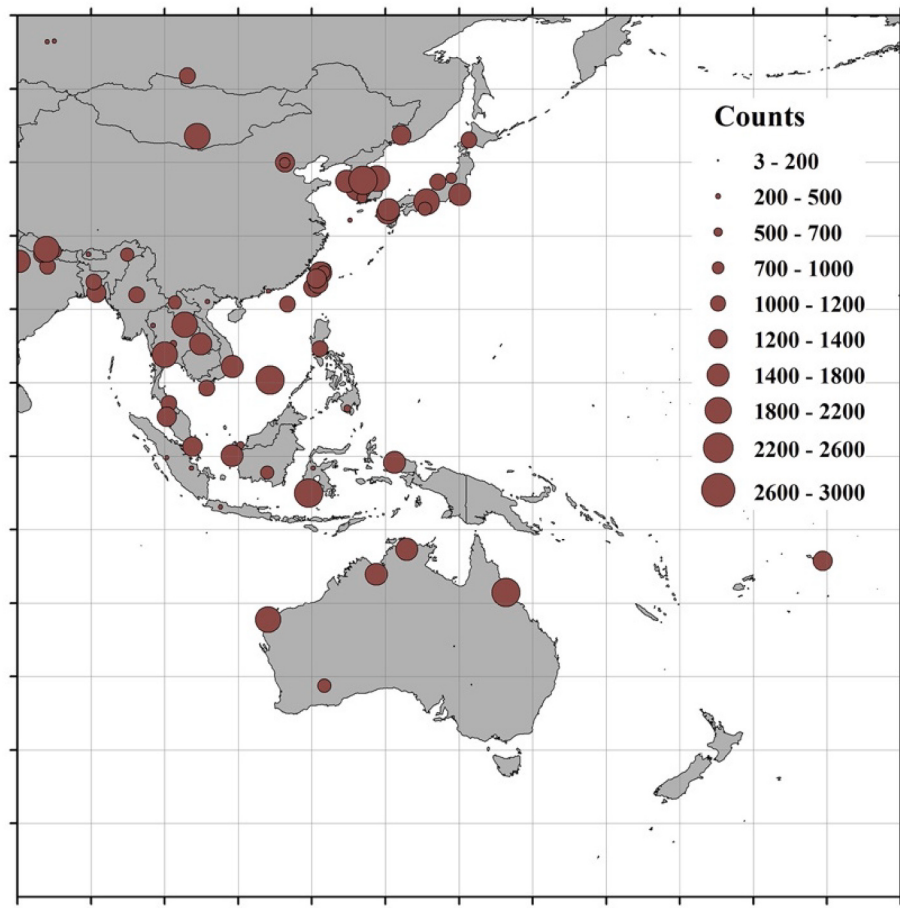


Fig. A1. The amount of data available for machine learning over the AERONET sites within the Himawari-8 AHI domain.

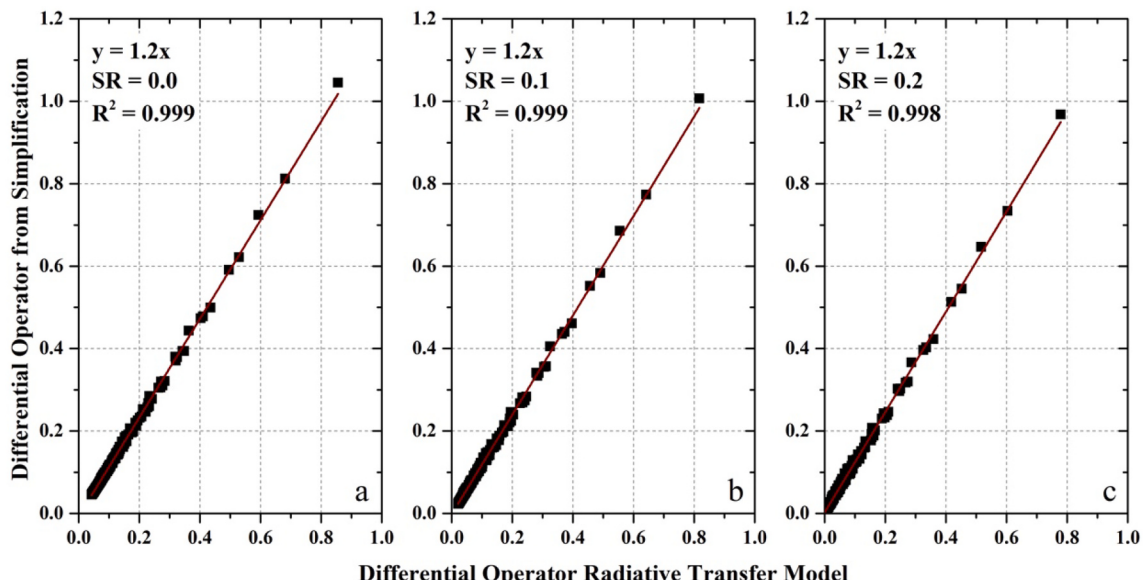


Fig. A2. The comparison of the differential operator ($0.46 \mu\text{m}$) simulated by the radiative transfer model (6SV) and calculated by the simplified equations (Eq. (4)). The simulation assumed a hazy AOD of 1.0 and a clear AOD of 0.1, with three surface reflectance are applied (0.1, 0.2, 0.3).

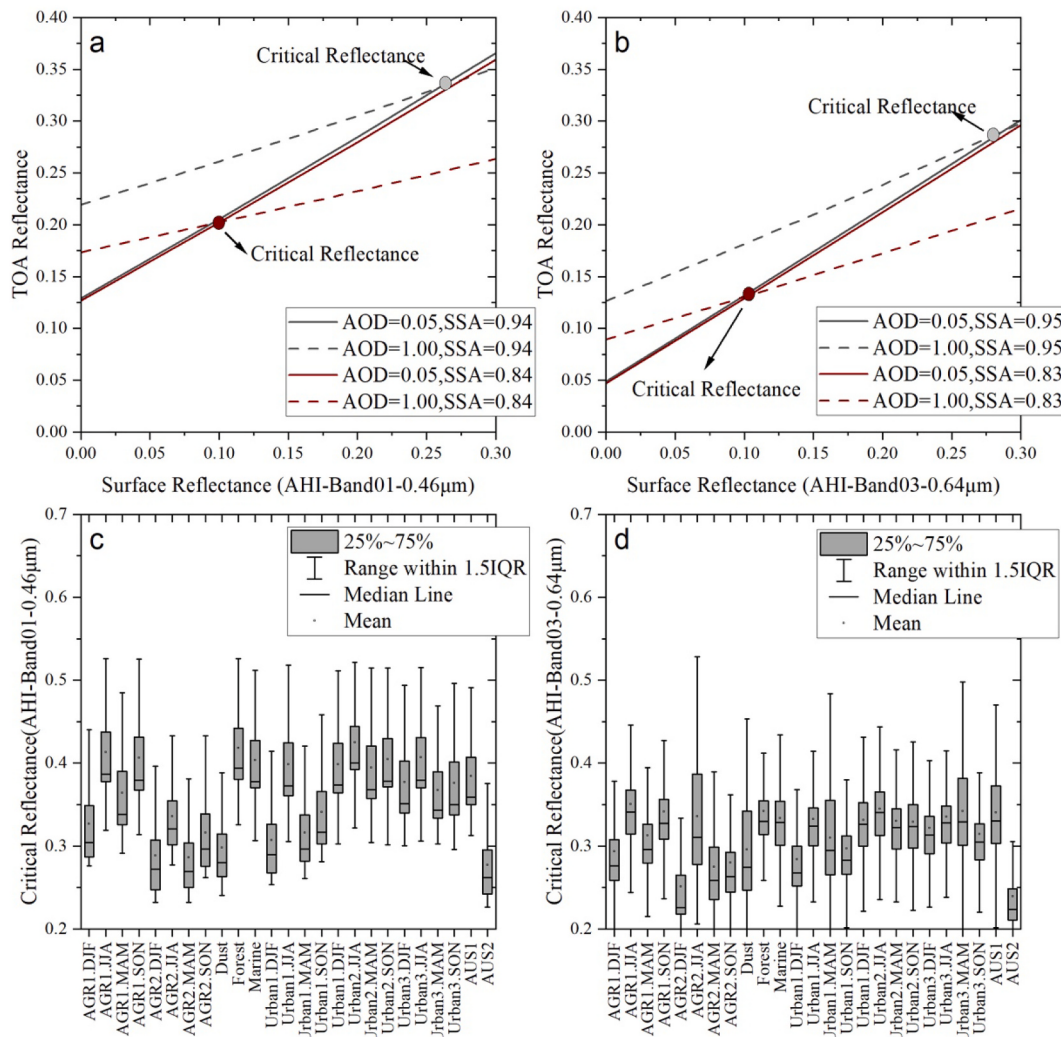


Fig. A3. (a-b) Simulations (solar zenith = 36° and AHI zenith = 48°) of the AHI TOA apparent reflectance under different AOD scenarios (0.05 and 1.00). Two different aerosol types (via SSA) and AHI bands ($0.46\text{ }\mu\text{m}$ and $0.64\text{ }\mu\text{m}$) are selected in the calculations. The points in the figure are the critical reflectance where AOD has approximately zero-contribution. (c-d) Box chart of critical reflectance for clustered aerosol models in Fig. 1. The range of the I-shaped line represents the range within the 1.5 interquartile range (IQR).

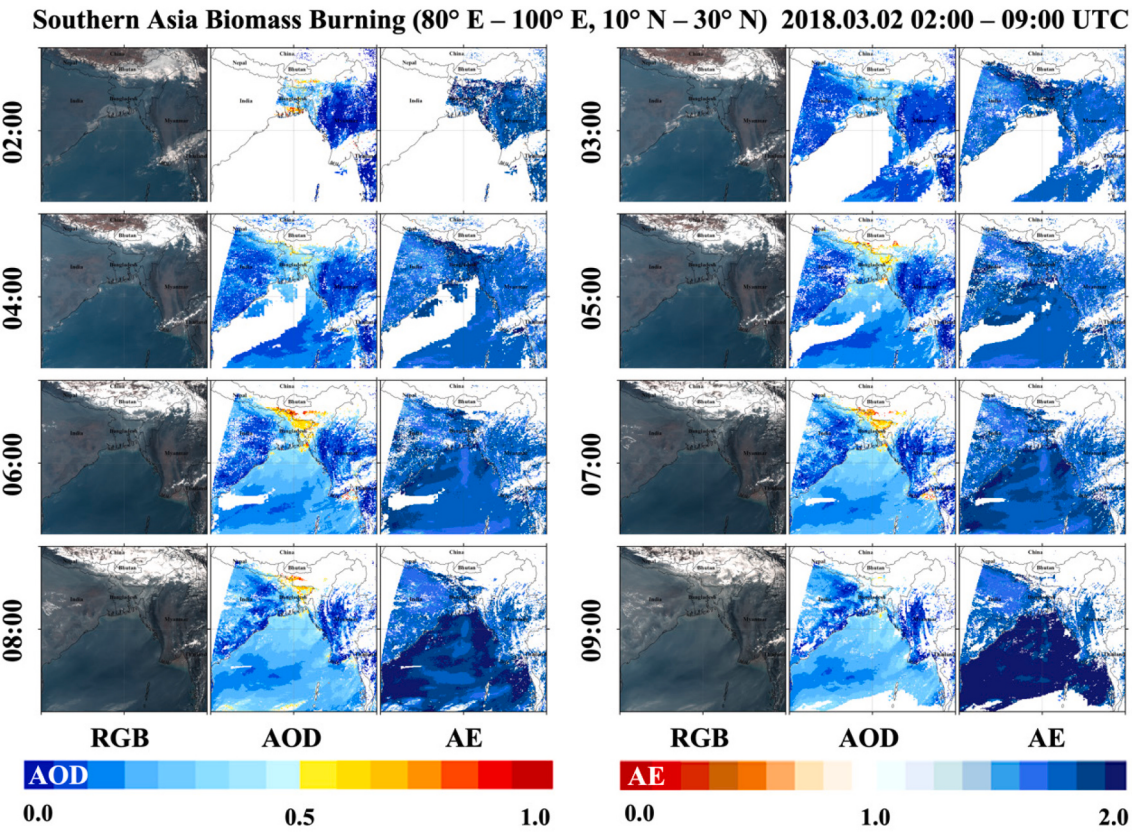


Fig. A4. Biomass burning (March 2nd, 2018) in southern Asia (80° E - 100° E, 10° N - 30° N) based on hourly (02:00 UTC – 09:00 UTC) level 2 operational AHI aerosol products (L2 ARP). From left to right are the RGB image of AHI, AOD patterns at $0.50\text{ }\mu\text{m}$ calculated by spectral AODs and their AE patterns, respectively.

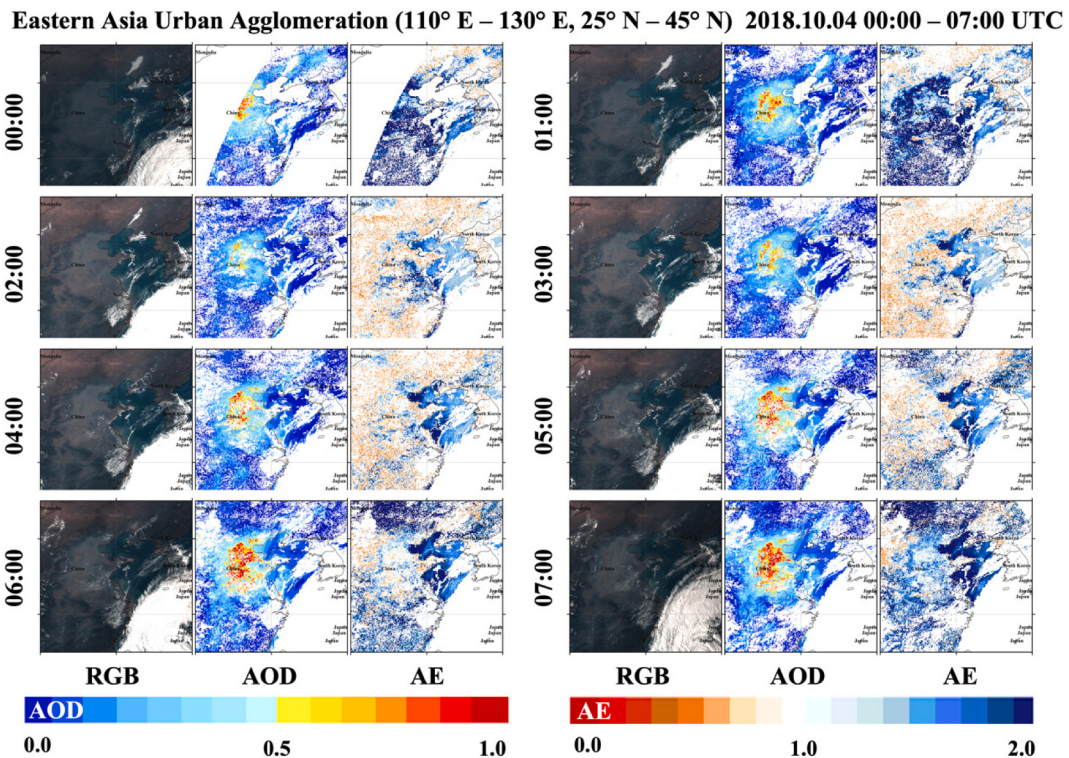


Fig. A5. Same as Fig. A3 but for urban agglomeration pollution (October 4th, 2018, 00:00 UTC – 07:00 UTC) in Eastern Asia (110° E - 130° E, 25° N – 45° N).

References

- Ångström, A., 1929. On the atmospheric transmission of sun radiation and on dust in the air. *Geogr. Ann.* 11, 156–166.
- Bao, F., Gu, X., Cheng, T., Wang, Y., Guo, H., Chen, H., Wei, X., Xiang, K., Li, Y., 2016. High-spatial-resolution aerosol optical properties retrieval algorithm using Chinese high-resolution earth observation satellite I. *IEEE Trans. Geosci. Remote Sens.* 54, 5544–5552.
- Breiman, L., 2001. Random forests. *Mach. Learn.* 45, 5–32.
- Charlson, R.J., Schwartz, S.E., Hales, J.M., Cess, R.D., Coakley, J.A., Hansen, J.E., Hofmann, D.J., 1992. Climate forcing by anthropogenic aerosols. *Science* 255, 423–430.
- Chen, A., Yang, J., He, Y., Yuan, Q., Li, Z., Zhu, L., 2022a. High spatiotemporal resolution estimation of AOD from Himawari-8 using an ensemble machine learning gap-filling method. *Sci. Total Environ.* 159673.
- Chen, X., Zhao, L., Zheng, F., Li, J., Li, L., Ding, H., Zhang, K., Liu, S., Li, D., de Leeuw, G., 2022. Neural Network AEROSol Retrieval for Geostationary Satellite (NNAeroG) based on temporal, spatial and spectral measurements. *Remote Sens.* 14, 980.
- Chen, X.F., de Leeuw, G., Arola, A., Liu, S.M., Liu, Y., Li, Z.Q., Zhang, K.N., 2020. Joint retrieval of the aerosol fine mode fraction and optical depth using MODIS spectral reflectance over northern and eastern China: artificial neural network method. *Remote Sens. Environ.* 249.
- Chen, Y., Fan, M., Li, M., Li, Z., Tao, J., Wang, Z., Chen, L., 2022c. Himawari-8/AHI aerosol optical depth detection based on machine learning algorithm. *Remote Sens.* 14, 2967.
- Choi, M., Kim, J., Lee, J., Kim, M., Park, Y.-J., Jeong, U., Kim, W., Hong, H., Holben, B., Eck, T.F., 2016. GOCCI yonsei aerosol retrieval (YAER) algorithm and validation during the DRAGON-NE Asia 2012 campaign. *Atmos. Meas. Tech.* 9, 1377–1398.
- Chu, D.A., Kaufman, Y.J., Ichoku, C., Remer, L.A., Tanre, D., Holben, B.N., 2002. Validation of MODIS aerosol optical depth retrieval over land. *Geophys. Res. Lett.* 29.
- Di Noia, A., Hasekamp, O.P., Wu, L.H., van Diedenhoven, B., Cairns, B., Yorks, J.E., 2017. Combined neural network/Phillips-tikhonov approach to aerosol retrievals over land from the NASA research scanning polarimeter. *Atmos. Meas. Tech.* 10, 4235–4252.
- Dubovik, O., Herman, M., Holdak, A., Lapyonok, T., Tanre, D., Deuze, J.L., Ducos, F., Sinyuk, A., Lopatin, A., 2011. Statistically optimized inversion algorithm for enhanced retrieval of aerosol properties from spectral multi-angle polarimetric satellite observations. *Atmos. Meas. Tech.* 4, 975–1018.
- Fan, C., Fu, G.L., Di Noia, A., Smit, M., Rietjens, J.H.H., Ferrare, R.A., Burton, S., Li, Z.Q., Hasekamp, O.P., 2019. Use of a neural network-based ocean body radiative transfer model for aerosol retrievals from multi-angle polarimetric measurements. *Remote Sens.* 11.
- Gao, J., Li, Y., Xie, Z., Hu, B., Wang, L., Bao, F., Fan, S., 2022. The impact of the aerosol reduction on the worsening ozone pollution over the Beijing-Tianjin-Hebei region via influencing photolysis rates. *Sci. Total Environ.* 821, 153197.
- Gao, J., Li, Y., Zhu, B., Hu, B., Wang, L., Bao, F., 2020. What have we missed when studying the impact of aerosols on surface ozone via changing photolysis rates? *Atmos. Chem. Phys.* 20, 10831–10844.
- Giles, D.M., Holben, B.N., Eck, T.F., Sinyuk, A., Smirnov, A., Slutsker, I., Dickerson, R., Thompson, A., Schaefer, J., 2012. An analysis of AERONET aerosol absorption properties and classifications representative of aerosol source regions. *J. Geophys. Res. Atmos.* 117.
- Giles, D.M., Sinyuk, A., Sorokin, M.G., Schafer, J.S., Smirnov, A., Slutsker, I., Eck, T.F., Holben, B.N., Lewis, J.R., Campbell, J.R., 2019. Advancements in the aerosol robotic network (AERONET) version 3 database—automated near-real-time quality control algorithm with improved cloud screening for sun photometer aerosol optical depth (AOD) measurements. *Atmos. Meas. Tech.* 12, 169–209.
- Hansen, J., Sato, M., Ruedy, R., 1997. Radiative forcing and climate response. *J. Geophys. Res. Atmos.* 102, 6831–6864.
- Hastie, T., Tibshirani, R., Friedman, J.H., Friedman, J.H., 2009. The elements of statistical learning: data mining, inference, and prediction. Springer.
- Holben, B.N., Eck, T.F., Slutsker, I.A., Tanre, D., Buis, J., Setzer, A., Vermote, E., Reagan, J.A., Kaufman, Y., Nakajima, T., 1998. AERONET—A federated instrument network and data archive for aerosol characterization. *Remote Sens. Environ.* 66, 1–16.
- Hsu, N.C., Tsay, S.C., King, M.D., Herman, J.R., 2004. Aerosol properties over bright-reflecting source regions. *IEEE Trans. Geosci. Remote Sens.* 42, 557–569.
- Hu, X.F., Belle, J.H., Meng, X., Wildani, A., Waller, L.A., Strickland, M.J., Liu, Y., 2017. Estimating PM2.5 concentrations in the conterminous United States using the random Forest approach. *Environ. Sci. Technol.* 51, 6936–6944.
- Huang, K., Xiao, Q., Meng, X., Geng, G., Wang, Y., Lyapustin, A., Gu, D., Liu, Y., 2018. Predicting monthly high-resolution PM2.5 concentrations with random forest model in the North China plain. *Environ. Pollut.* 242, 675–683.
- Jackson, J.M., Liu, H.Q., Laszlo, I., Kondragunta, S., Remer, L.A., Huang, J.F., Huang, H.C., 2013. Suomi-NPP VIIRS aerosol algorithms and data products. *J. Geophys. Res. Atmos.* 118, 12673–12689.
- Jiang, T., Chen, B., Chan, K.K.Y., Xu, B., 2019. Himawari-8/AHI and MODIS aerosol optical depths in China: evaluation and comparison. *Remote Sens.* 11, 1011.
- Kang, Y., Kim, M., Kang, E., Cho, D., Im, J., 2022. Improved retrievals of aerosol optical depth and fine mode fraction from GOCCI geostationary satellite data using machine learning over East Asia. *ISPRS J. Photogramm. Remote Sens.* 183, 253–268.
- Lanzaco, B.L., Olcese, L.E., Palancar, G.G., Toselli, B.M., 2017. An improved aerosol optical depth map based on machine-learning and MODIS data: development and application in South America. *Aerosol Air Qual. Res.* 17, 1623–1636.
- Lary, D.J., Remer, L., MacNeill, D., Roscoe, B., Paradise, S., 2009. Machine learning and bias correction of MODIS aerosol optical depth. *IEEE Geosci. Remote Sens. Lett.* 6, 694–698.
- Lee, H.J., Liu, Y., Coull, B.A., Schwartz, J., Koutrakis, P., 2011. A novel calibration approach of MODIS AOD data to predict PM2.5 concentrations. *Atmos. Chem. Phys.* 11, 7991–8002.
- Lee, J., Kim, J., Song, C.H., Ryu, J.H., Ahn, Y.H., Song, C.K., 2010. Algorithm for retrieval of aerosol optical properties over the ocean from the Geostationary Ocean color imager. *Remote Sens. Environ.* 114, 1077–1088.
- Letu, H., Yang, K., Nakajima, T.Y., Ishimoto, H., Nagao, T.M., Riedi, J., Baran, A.J., Ma, R., Wang, T., Shang, H., 2020. High-resolution retrieval of cloud microphysical properties and surface solar radiation using Himawari-8/AHI next-generation geostationary satellite. *Remote Sens. Environ.* 239, 111583.
- Levy, R.C., Mattoe, S., Munchak, L.A., Remer, L.A., Sayer, A.M., Patadia, F., Hsu, N.C., 2013. The collection 6 MODIS aerosol products over land and ocean. *Atmos. Meas. Tech.* 6, 2989–3034.
- Lim, H., Choi, M., Kim, J., Kasai, Y., Chan, P.W., 2018. AHI/Himawari-8 yonsei aerosol retrieval (YAER): algorithm, validation and merged products. *Remote Sens.* 10, 699.
- Lin, C.Q., Li, Y., Yuan, Z.B., Lau, A.K.H., Li, C.C., Fung, J.C.H., 2015. Using satellite remote sensing data to estimate the high-resolution distribution of ground-level PM2.5. *Remote Sens. Environ.* 156, 117–128.
- Lyapustin, A., Wang, Y., Korkin, S., Huang, D., 2018. MODIS collection 6 MAIAC algorithm. *Atmos. Meas. Tech.* 11, 5741–5765.
- Ma, Z.W., Hu, X.F., Sayer, A.M., Levy, R., Zhang, Q., Xue, Y.G., Tong, S.L., Bi, J., Huang, L., Liu, Y., 2016. Satellite-based spatiotemporal trends in PM2.5 concentrations: China, 2004–2013. *Environ. Health Perspect.* 124, 184–192.
- Martonchik, J.V., Diner, D.J., Kahn, R.A., Ackerman, T.P., Verstraete, M.E., Pinty, B., Gordon, H.R., 1998. Techniques for the retrieval of aerosol properties over land and ocean using multiangle imaging. *IEEE Trans. Geosci. Remote Sens.* 36, 1212–1227.
- Myhre, G., Samset, B.H., Schulz, M., Balkanski, Y., Bauer, S., Berntsen, T.K., Bian, H., Bellouin, N., Chin, M., Diehl, T., Easter, R.C., Feichter, J., Ghan, S.J., Hauglustaine, D., Iversen, T., Kinne, S., Kirkevag, A., Lamarque, J.F., Lin, G., Liu, X., Lund, M.T., Luo, G., Ma, X., van Noije, T., Penner, J.E., Rasch, P.J., Ruiz, A., Seland, O., Skeie, R.B., Stier, P., Takemura, T., Tsigaridis, K., Wang, P., Wang, Z., Xu, L., Yu, H., Yu, F., Yoon, J.H., Zhang, K., Zhang, H., Zhou, C., 2013. Radiative forcing of the direct aerosol effect from AeroCom phase II simulations. *Atmos. Chem. Phys.* 13, 1853–1877.
- Nanda, S., de Graaf, M., Vreekwind, J.P., ter Linden, M., Sneep, M., de Haan, J., Levelt, P.F., 2019. A neural network radiative transfer model approach applied to the tropospheric monitoring instrument aerosol height algorithm. *Atmos. Meas. Tech.* 12, 6619–6634.
- Niang, A., Badran, F., Moulin, C., Crepon, M., Thiria, S., 2006. Retrieval of aerosol type and optical thickness over the Mediterranean from SeaWiFS images using an automatic neural classification method. *Remote Sens. Environ.* 100, 82–94.
- Omar, A.H., Won, J.G., Winker, D.M., Yoon, S.C., Dubovik, O., McCormick, M.P., 2005. Development of global aerosol models using cluster analysis of aerosol robotic network (AERONET) measurements. *J. Geophys. Res. Atmos.* 110.
- Qin, W.M., Fang, H.J., Wang, L.C., Wei, J., Zhang, M., Su, X., Bilal, M., Liang, X., 2021. MODIS high-resolution MAIAC aerosol product: global validation and analysis. *Atmos. Environ.* 264.
- Ramanathan, V., Crutzen, P.J., Kiehl, J.T., Rosenfeld, D., 2001. Atmosphere - aerosols, climate, and the hydrological cycle. *Science* 294, 2119–2124.
- Ramanathan, V., Ramana, M.V., 2005. Persistent, widespread, and strongly absorbing haze over the Himalayan foothills and the indo-Gangetic Plains. *Pure Appl. Geophys.* 162, 1609–1626.
- Sayer, A.M., Munchak, L.A., Hsu, N.C., Levy, R.C., Bettenhausen, C., Jeong, M.J., 2014. MODIS collection 6 aerosol products: comparison between Aqua's e-deep blue, dark target, and "merged" data sets, and usage recommendations. *J. Geophys. Res. Atmos.* 119, 13965–13989.
- Schuster, G.L., Dubovik, O., Holben, B.N., 2006. Angstrom exponent and bimodal aerosol size distributions. *J. Geophys. Res. Atmos.* 111.
- She, L., Zhang, H.K.K., Li, Z.Q., de Leeuw, G., Huang, B., 2020. Himawari-8 aerosol optical depth (AOD) retrieval using a deep neural network trained using AERONET observations. *Remote Sens.* 12.
- Shindell, D.T., Lamarque, J.F., Schulz, M., Flanner, M., Jiao, C., Chin, M., Young, P.J., Lee, Y.H., Rotstayn, L., Mahowald, N., Milly, G., Faluvegi, G., Balkanski, Y., Collins, W.J., Conley, A.J., Dalsoren, S., Easter, R., Ghan, S., Horowitz, L., Liu, X., Myhre, G., Nagashima, T., Naik, V., Rumbold, S.T., Skeie, R., Sudo, K., Szopa, S., Takemura, T., Voulgarakis, A., Yoon, J.H., Lo, F., 2013. Radiative forcing in the ACCMIP historical and future climate simulations. *Atmos. Chem. Phys.* 13, 2939–2947.
- Song, C., Park, M., Lee, K., Ahn, H., Lee, Y., Kim, J., Han, K., Kim, J., Ghim, Y., Kim, Y., 2008. An investigation into seasonal and regional aerosol characteristics in East Asia using model-predicted and remotely-sensed aerosol properties. *Atmos. Chem. Phys.* 8, 6627–6654.
- Stafoggia, M., Bellander, T., Bucci, S., Davoli, M., de Hoogh, K., de Donato, F., Gariazzo, C., Lyapustin, A., Michelozzi, P., Renzi, M., Scorticichini, M., Shtain, A., Viegi, G., Kloog, I., Schwartz, J., 2019. Estimation of daily PM10 and PM2.5 concentrations in Italy, 2013–2015, using a spatiotemporal land-use random-forest model. *Environ. Int.* 124, 170–179.
- Su, T., Laszlo, I., Li, Z., Wei, J., Kalluri, S., 2020. Refining aerosol optical depth retrievals over land by constructing the relationship of spectral surface reflectances through deep learning: application to Himawari-8. *Remote Sens. Environ.* 251, 112093.
- Taylor, M., Kazadzis, S., Tsakiri, A., Gkikas, A., Amiridis, V., 2014. Satellite retrieval of aerosol microphysical and optical parameters using neural networks: a new

- methodology applied to the Sahara desert dust peak. *Atmos. Meas. Tech.* 7, 3151–3175.
- van Donkelaar, A., Martin, R.V., Brauer, M., Kahn, R., Levy, R., Verduzco, C., Villeneuve, P.J., 2010. Global estimates of ambient fine particulate matter concentrations from satellite-based aerosol optical depth: development and application. *Environ. Health Perspect.* 118, 847–855.
- Vermote, E.F., Tanre, D., Deuze, J.L., Herman, M., Morcrette, J.J., 1997. Second simulation of the satellite signal in the solar spectrum, 6S: an overview. *IEEE Trans. Geosci. Remote Sens.* 35, 675–686.
- Vucetic, S., Han, B., Mi, W., Li, Z.Q., Obradovic, Z., 2008. A data-mining approach for the validation of aerosol retrievals. *IEEE Geosci. Remote Sens. Lett.* 5, 113–117.
- Wei, J., Huang, W., Li, Z.Q., Xue, W.H., Peng, Y.R., Sun, L., Cribb, M., 2019. Estimating 1-km-resolution PM2.5 concentrations across China using the space-time random forest approach. *Remote Sens. Environ.* 231.
- Yu, H., Kaufman, Y.J., Chin, M., Feingold, G., Remer, L.A., Anderson, T.L., Balkanski, Y., Bellouin, N., Boucher, O., Christopher, S., DeCola, P., Kahn, R., Koch, D., Loeb, N., Reddy, M.S., Schulz, M., Takemura, T., Zhou, M., 2006. A review of measurement-based assessments of the aerosol direct radiative effect and forcing. *Atmos. Chem. Phys.* 6, 613–666.
- Yumimoto, K., Nagao, T.M., Kikuchi, M., Sekiyama, T.T., Murakami, H., Tanaka, T.Y., Ogi, A., Irie, H., Khatri, P., Okumura, H., Arai, K., Morino, I., Uchino, O., Maki, T., 2016. Aerosol data assimilation using data from Himawari-8, a next-generation geostationary meteorological satellite. *Geophys. Res. Lett.* 43, 5886–5894.
- Zhang, Z.Y., Wu, W.L., Fan, M., Tao, M.H., Wei, J., Jin, J., Tan, Y.H., Wang, Q., 2019. Validation of Himawari-8 aerosol optical depth retrievals over China. *Atmos. Environ.* 199, 32–44.